Selective and Efficient Light-Driven CO_2 Reduction to CO with a Heptacoordinated Polypyridine Iron(II) Catalyst

Federico Droghetti,[‡] *Florian Lemken,*[†] *Lubomir Rulisek,**[,†] *Albert Ruggi,**[⁋] *Mirco Natali* *[,‡]

[‡] Department of Chemical, Pharmaceutical and Agricultural Sciences, University of Ferrara, Via L. Borsari 46, 44121 Ferrara, Italy.

[†] Institute of Organic Chemistry and Biochemistry of the Czech Academy of Sciences, Flemingovo náměstí 2, 160 00, Praha 6, Czech Republic.

[⁋] Department of Chemistry, University of Fribourg, Chemin du Musée 9, 1700 Fribourg, Switzerland.

KEYWORDS. Carbon dioxide reduction; iron polypyridine complexes; selectivity; light-driven processes; mechanistic insight; quantum chemical calculations.

ABSTRACT

The selective generation of carbon-based products in the presence of proton donors currently represents one of the major goals in the catalysis of the CO_2 reduction reaction (CO_2RR). Within this framework, the iron complex of the 1-([2,2'-bipyridin]-6-yl)-N-([2,2'-bipyridin]-6-ylmethyl)-N-(pyridin-2-ylmethyl) methanamine ligand (DBPy-PyA) turns out to be a selective and efficient catalyst to promote the conversion of CO_2 into CO. In the present work, we report a detailed investigation of the CO_2RR by this metal complex joining experimental and computational studies. Efficient formation of CO (selectivity >90%) was attained under electrochemical conditions (applied potential of −2.0 V vs Fc^+/Fc) using trifluoroethanol as the proton donor, which provides the best balance, among those tested, in terms of Lewis and Brønsted acidity. This is indeed instrumental in accelerating CO_2 activation, while minimizing the parallel generation of hydrogen by-product. The high activity and selectivity towards CO formation is shown to arise from i) the ability of the ligand to assist via intramolecular routes the formation of the metallacarboxylic acid catalytic intermediate, ii) the favorable and almost barrierless detachment of the CO product from the putative iron(II) carbonyl intermediate, and iii) the weak tendency of the two-electron reduced complex to form the metal-hydride species. The CO_2RR by the titled complex was further investigated under light-driven catalytic conditions with $[Ru(bpy)_3]^{2+}$ (bpy = 2,2'-bipyridine) as the sensitizer and *N*,*N*-diisopropylethylamine (DIPEA) as the electron donor, leading to unprecedented performances under 1 sun irradiation (0.85 mL CO per mL of solution, quantum yield of 9.4%, selectivity >97%, solely limited by degradation of the sensitizer). Transient absorption spectroscopy suggests that, for the three-component photochemical system examined, catalyst activation by the photogenerated reductant represents the rate-determining step of the photosynthetic process. With this information in hand,

by carefully modulating the photon flux, we succeeded to achieve a more than three-fold enhancement in the quantum yield of CO formation (up to 28%). All in all, our study showcases the great, but often underestimated, potential of molecular catalysis to target efficient and selective transformations.

INTRODUCTION

The reduction of carbon dioxide into carbon-based products (CO_2 reduction reaction, CO_2RR) poses as one of the most challenging solutions to the global energy issue, since it gives the possibility to reduce the level of CO_2 while simultaneously generating fuels or industrially relevant intermediates.[1-3] Seemingly simple at first glance, the CO_2RR displays both thermodynamic and kinetic hurdles. The reduction of CO_2 to its radical anion requires large potentials[4,5] and lower thermodynamic requirements can only be achieved by employing a proton donor.[6,7] However, the complexity of the reaction mechanism increases and the use of a catalyst becomes imperative to get control over the multiple electron and proton transfers involved.[8-17] Moreover, the requirement of proton donation introduces selectivity issues associated with the competition between the CO_2RR and the hydrogen evolution reaction (HER).[18] Hence, the quest for molecular catalysts which are both efficient and selective towards the generation of single carbon-based products is of paramount importance. In this regard, several approaches have been particularly pursued to challenge selectivity issues. Some of those have involved, e.g., metal exchange,[19] modification of the ligand scaffold,[20] and change of the solvent mixture.[21]

We have been recently involved in the preparation of cobalt polypyridine complexes and have employed them as catalysts for the HER under both electrochemical and light-driven conditions.[22-31] We have reported on a variety of cobalt complexes based on the 1-([2,2'-bipyridin]-6-yl)-N-([2,2'-bipyridin]-6-ylmethyl)-N-(pyridin-2-ylmethyl) methanamine ligand (DBPy-PyA), featuring an uncommon heptacoordinated structure in the solid state (see the prototype complex **CoL^{MeOH}** in Chart 1a).[27-31] The key design motifs within these metal complexes are inspired by nature.[32] They indeed exploit the redox-active character of the DBPy-PyA ligand that acts as electron reservoir, akin to the ligand environment of Fe-only

hydrogenases,[33,34] which is particularly instrumental to access the one- and two-electron reduced species of the catalyst at reasonably low potentials.[35] Furthermore, the presence of dangling pyridine groups facilitates ligand protonation, which assists the formation of the relevant catalytic intermediates as well as the elimination of the H_2 molecule,[28] akin to the pendant amine of FeFe hydrogenases (Chart 1b).[33,36] Thanks to these interesting properties, for a cobalt derivative (Chart 1c) outstanding performances were indeed recorded[29] towards light-driven hydrogen evolution with $[Ru(bpy)_3]^{2+}$ (where bpy = 2,2'-bipyridine) as the sensitizer and ascorbate as the electron donor. Furthermore, we have recently demonstrated that the cobalt complex (**CoL^{MeOH}**) is also active towards the CO_2RR when the catalysis is conducted in acetonitrile solution in the presence of H_2O as a proton donor.[37] Under these conditions, however, the major products are formate and/or hydrogen, suggesting a strong preference of the cobalt complex for the hydride catalytic pathway. Replacing the cobalt center with iron (**FeL^{MeOH}**, complex, Chart 1a) caused a drastic switch in the catalytic behavior, resulting in preferential CO formation when the catalysis was conducted in acetonitrile/H_2O mixtures under both electrochemical and light-driven conditions.[37]

In the present work, we aim at a detailed investigation of the catalytic activity of **FeL^{MeOH}** towards the CO_2RR. We show that, combining electrochemical and computational studies, we have obtained a comprehensive picture of the catalytic mechanisms towards the CO_2RR and the competitive HER. We further exploit these findings by exploring the ability of **FeL^{MeOH}** to reach efficient and selective generation of CO under photochemical conditions, in combination with $[Ru(bpy)_3]^{2+}$ as the sensitizer and *N*,*N*-diisopropylethylamine (DIPEA) as the electron donor. Remarkably, by merging catalytic studies and transient absorption spectroscopy results we have been able to identify both the turnover limiting factors and the rate-determining

step of the light-driven catalytic process. Utilizing this knowledge, we carefully modulated the experimental conditions and finally succeeded in obtaining quantitative (up to 188 µmol of CO, corresponding to up to 0.85 mL of gaseous product per mL of solution), selective (up to 97%), and efficient (quantum yield up to 28%) conversion of CO_2 into CO in a single run.

Chart 1. a) Molecular structures of complexes **CoL^{MeOH}** and **FeL^{MeOH}**; b) bioinspired features of complexes based on the DBPy-PyA ligand, c) previous report on HER by cobalt complexes based on the DBPy-PyA ligand, and d) outline of this work.

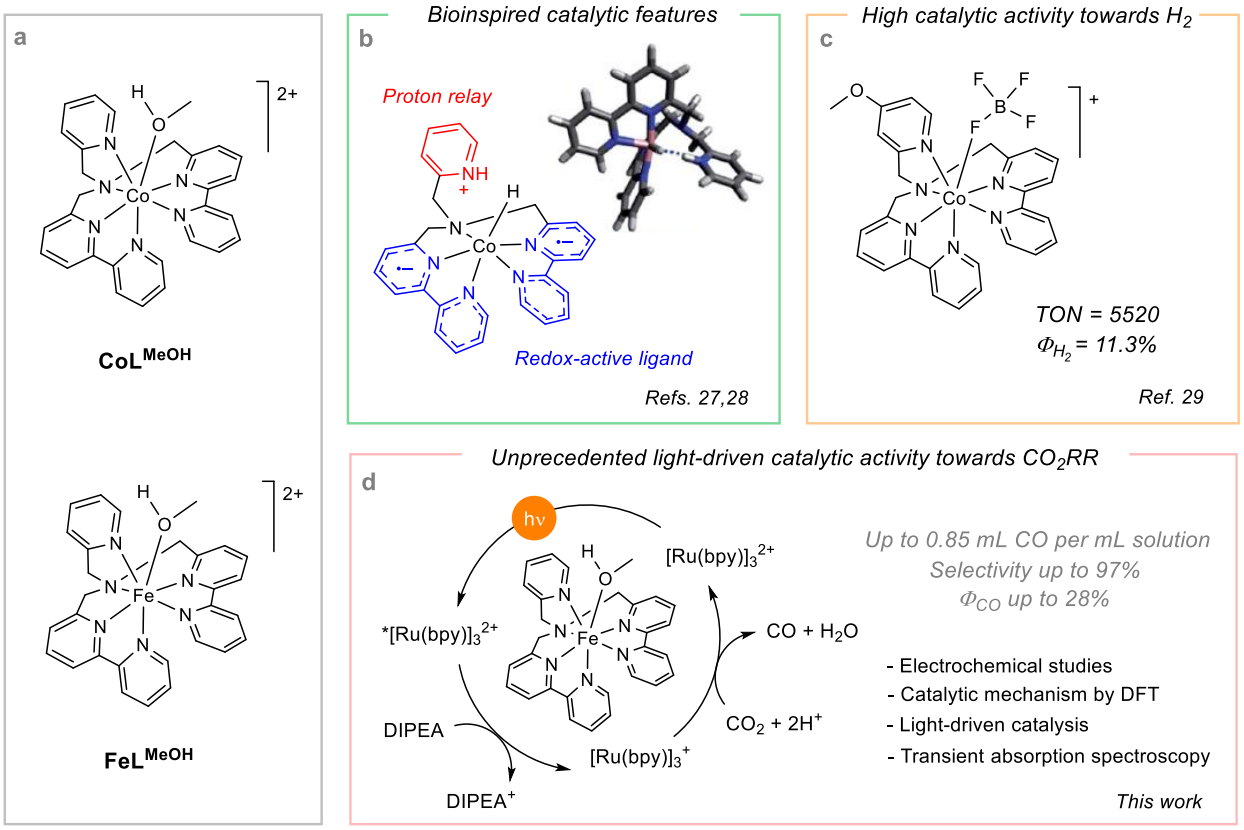

RESULTS AND DISCUSSION

Electrocatalytic CO_2 reduction

The cyclic voltammetry of complex **FeL^{MeOH}** in anhydrous acetonitrile displays two reversible reduction processes taking place at $E_{1/2}$ of −1.65 and −1.85 V vs Fc^+/Fc, associated with formal Fe(II)/Fe(I) and Fe(I)/Fe(0) processes, respectively. The two reduction potentials were computed at −1.65 and −1.96 V (vs Fc^+/Fc couple, for details see the Supporting Information, Section 3), in very good agreement with the experimental data, providing additional confidence in our calibrated computational protocols.[38-42] Since CO_2 activation requires the opening of a coordination site, in the next step, we investigated the stability of the binding of the seventh ligand L' (either the original methanol, acetonitrile or the proton donors employed in the catalytic studies) to the hexacoordinated **FeL** complex. The computed binding free energies are presented in Table S2. It can be clearly seen that binding of solvent molecules to the catalyst is close to ergoneutral (mostly within 1 kcal·mol^{-1}), and often even slightly positive (endergonic). This indicates an (observable) equilibrium between the solvent-bound and unbound forms of the catalyst. After the first reduction, the calculated binding free energies increase towards positive values (Table S3) which shifts the above equilibrium towards a form of the catalysts without a bound solvent molecule. Thus, the reduction promotes the opening of the CO_2 coordination site, activating the complex towards substrate binding. Løwdin population analysis (Table S5) indicates that both reduction steps take place on the DBPy-PyA ligand, namely the bipyridine moieties, with the spins of the unpaired electrons aligning in a parallel fashion. Spectroelectrochemistry measurements further supported these findings.[37] In summary, by correlating computations and experiments, we showed that **FeL^{MeOH}** is converted into **FeL^{ACN}** upon dissolution in acetonitrile and changes from a heptacoordinated species in a quintet state to a hexacoordinated species in a triplet state upon two-electron reduction. While an open-shell singlet ground state has been reported for the Fe(0) species of some polypyridine iron

complexes,[9,10,43] the triplet ground state predicted for the Fe(0) species of **FeL^{MeOH}** aligns with findings reported by Wu et al. for more similar complexes.[44]

In the presence of CO_2, both reduction waves experience an increase in current due to the ability of both electrogenerated Fe(I) and Fe(0) to bind CO_2 (Figure 1). Addition of H_2O as a proton donor (pK_a ~ 38 in acetonitrile)[45] leads to further enhancement of the catalytic currents at both reduction waves, associated with improved kinetics for CO_2 activation. On the other hand, negligible reactivity with H_2O in the absence of CO_2 was recorded for both electrogenerated Fe(I) and Fe(0) species,[37] showing that **FeL^{MeOH}** is a competent catalyst to promote selective CO_2 reduction to CO. Two catalytic mechanisms for CO_2 reduction to CO can be hypothesized depending on the catalytic wave (and applied potential): an ECEC at the Fe(II)/Fe(I) step and an EECC mechanism at the Fe(I)/Fe(0), where E and C are electron-transfer and chemical steps, respectively (Scheme 1). In this regard, the observation for both waves of constant catalytic half-wave potentials ($E_{cat,1}$, $E_{cat,2}$) as a function of both scan rate and H_2O content[37] indicates that the first chemical step, namely CO_2 activation, represents the rate-determining step for both mechanisms when H_2O is used as the proton donor.[46] We should recall that addition of up to 10% H_2O to **FeL^{MeOH}** in acetonitrile resulted in a change of the absorption spectrum associated with replacement of the apical acetonitrile ligand with H_2O, i.e., the preferential formation of a **FeL^{H_2O}** complex,[37] as supported by calculated binding free energies of the respective ligands (Table S2). Controlled potential electrolysis (CPE) experiments at −2.0 V vs Fc^+/Fc finally confirm that CO represents the major electrocatalytic product with a selectivity of 76.5% at 10% H_2O. An increase in selectivity for CO up to a value of 84.3% is recorded at lower water content (i.e., 1% H_2O), but at the expenses of catalyst stability (total Faradaic efficiency of ca 40%).[37]

Scheme 1. Proposed catalytic mechanism consistent with the electrochemical data for a) CO_2 reduction to CO and b) proton reduction and formate formation by complex **FeL^{MeOH}** in acetonitrile in the presence of a proton donor (L' stands for the seventh ligand).

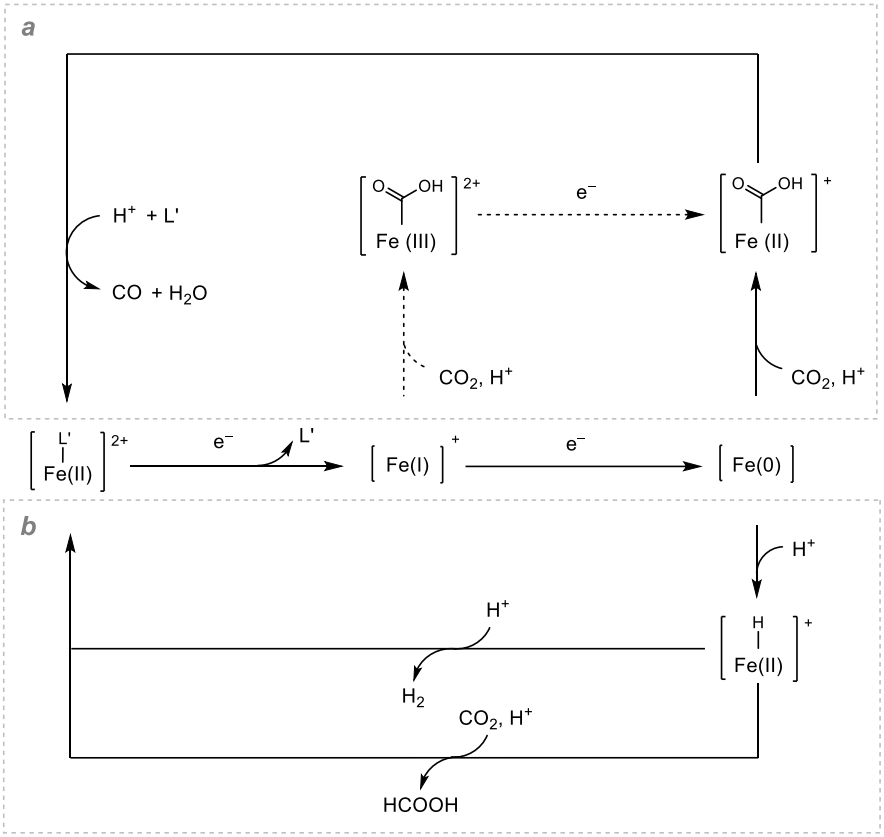

Starting from these premises, we investigated in more detail the effect of the proton source on the CO_2RR catalyzed by the **FeL^{MeOH}** complex in acetonitrile. To that end, we examined two alternative proton donors of increasing acidity, namely trifluoroethanol (TFE) and phenol (PhOH) featuring pK_a values of 35.4 and 29.1 in acetonitrile, respectively.[45,47] Figure 1a depicts the cyclic voltammetry (CV) of the complex in CO_2-saturated acetonitrile in the presence of 1 M proton donor. Akin to H_2O, two catalytic waves can be appreciated, associated with the reactivity of both the Fe(I) and Fe(0) species with CO_2 in the presence of both TFE and PhOH (in the case of PhOH the first wave is poorly defined due to the superposition with the second

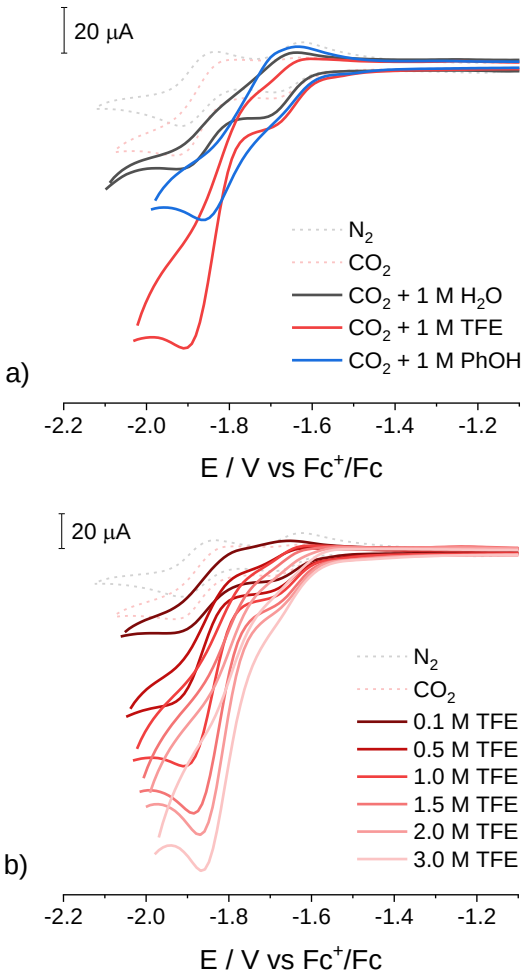

Figure 1. CV of 1 mM complex **FeL^{MeOH}** in acetonitrile a) under N_2, CO_2, and CO_2 with 1 M proton donor, and b) under N_2, CO_2, and CO_2 at different TFE concentrations; CVs were recorded at 0.1 V/s with a glassy carbon as the working electrode with 0.1 M $TBAPF_6$ as the supporting electrolyte.

catalytic event). This suggests that similar catalytic mechanisms can be envisioned with all proton donors (Scheme 1). Notably, the current enhancement at the Fe(I)/Fe(0) step is larger with TFE and PhOH (i_{cat}/i_p = 9.2 and 5.1 for TFE and PhOH, respectively) than H_2O (i_{cat}/i_p = 3.5) suggesting improved kinetics with stronger acids and a more pronounced ability of the TFE

adjutant to selectively trigger the EECC mechanism. In addition, the half-wave potential $E_{cat,2}$ (calculated at the inflection point of the catalytic wave)[47] experiences a progressive, positive shift in the order −1.85, −1.83, and −1.80 V vs Fc^+/Fc for H_2O, TFE, and PhOH, respectively, following the trend in the pK_a. This suggests a non-negligible effect of the proton donor on the catalytic process.

Inspection of the effects of the concentration of each proton donor and of the scan rate on the CV response reveals further mechanistic information on the CO_2RR catalysis by **FeL^{MeOH}**. Figure 1b displays the CVs obtained at different concentrations of TFE at a scan rate of 0.1 V/s, while the CVs at variable scan rates are reported in the Supporting Information (Figure S2-S8). Similar to what was observed for H_2O as the proton donor,[37] only small dependency on the TFE concentration was recorded for the Fe(II)/Fe(I) process. We only observed weak enhancements of the current, a small increase in reversibility at fast scan rates, and $E_{cat,1} \sim -1.65$ V vs Fc^+/Fc which was otherwise identical to the $E_{1/2}$ of the Fe(II)/Fe(I) couple in the absence of CO_2. This is consistent with the sluggish reactivity of the Fe(I) species with CO_2 and an intrinsic slowness (and inefficiency) of the ECEC pathway. On the other hand, a sharp increase in the catalytic current at the Fe(I)/Fe(0) reduction is apparent and dependent on the concentration of TFE, consistent with an efficient EECC catalytic process, particularly at larger TFE loadings. Only minor changes in the absorption spectrum of **FeL^{MeOH}** are observed in acetonitrile upon addition of TFE (Figure S9), likely originating from the weak TFE binding at the iron center. Thus, within the proposed EECC mechanism, removal of the preferentially bound acetonitrile ligand (Scheme 1) is herein expected before CO_2 activation. The catalytic half-wave potential ($E_{cat,2}$) is constant at all scan rates and identical to the $E_{1/2}$ of the Fe(I)/Fe(0) couple in the absence of CO_2 (−1.85 V vs Fc^+/Fc) for concentrations of 0.1 and 0.5 M TFE (Figure S10), consistent with a

rate-determining CO_2 activation step, as observed with H_2O as the proton donor. A positive shift can be observed at higher TFE concentrations (> 1 M) and slow scan rates (Figure S10), which can be explained assuming an improved reactivity of the electrogenerated Fe(0) species with TFE at high loadings (as evidenced by the CV analysis conducted under N_2, Figure S11). Interestingly, anodic peaks at ca −1.2 and −1.4 V vs Fc^+/Fc at high TFE concentrations (> 1 M) and fast scan rates (> 0.3 V/s) can be observed during the return scan (see Figure S12-S18), potentially assignable to the re-oxidation of catalytic intermediates which have not turned over due to rapid scan reversal.[49] This evidence is consistent with the highest catalytic currents measured with TFE, indicating a faster CO_2 binding step than observed with H_2O, as a result of the increased acidity of the proton donor.

When using PhOH as the proton source (see Figure S19-S25 of the Supporting Information), a prominent shift of the catalytic half-wave potential $E_{cat,2}$ is observed (Figure S27) This can be rationalized by considering the reactivity of the electrogenerated Fe(0) with PhOH, as expected based upon the highest pK_a among the series of acids tested (see Figure S28 for the CVs of **FeL^{MeOH}** with PhOH under N_2). More importantly, while a similar current enhancement with both TFE and PhOH is observed at 0.1 M proton donor ($i_{cat}/i_p \sim 3.7$), substantially lower current increases are measured upon further addition of PhOH (Figure S19). In this regard, the absorption spectra of **FeL^{MeOH}** in acetonitrile evidence the growth of a broad band in the red portion of the visible spectrum upon addition of PhOH (Figure S26), suggesting a non-innocent role of the proton donor. Likely, the increased presence of phenolate compared to other conjugated bases (either from protonation of the DBPy-PyA ligand or the solvent) facilitates the formation of an equilibrium between **FeL^{ACN}** and a phenolate adduct. For this adduct, DFT calculations predict considerably increased stability against detachment of phenolate

($\Delta_b G(^5[LFe\text{-}OPh]^+) = -17.5$ kcal·mol^{-1}) compared to other solvent ligands (see Table S2 and S3). This indicates a more sluggish removal of this solvent ligand slowing down CO_2 activation and catalysis at high PhOH concentrations.

CPE experiments were then performed to determine the reduction products using 1 mM **FeL^{MeOH}** as the catalyst in CO_2-saturated acetonitrile in combination with the three different proton donors. The Faradaic efficiencies (FE) attained after 2 h electrolysis at −2.0 V vs Fc^+/Fc and 1 M proton donor are displayed in Figure 2, while the numerical data in terms of both FE and selectivity, under all tested conditions, are summarized in Table 1.

Comparison of the CPE data at a fixed concentration of 1 M proton donor (Entries 2,5,8 in Table 1) shows that replacing H_2O with TFE mainly leads to an increase in stability of the catalytic system (total FE of 43.4% and 85% in H_2O and TFE, respectively), while no macroscopic differences are observed in terms of product distribution, with the system maintaining high selectivity towards the CO_2 reduction to CO (> 86%). This suggests that, under these conditions, TFE is considerably stronger than H_2O as a proton donor, accelerating CO_2 activation and catalysis, but at the same time it is sufficiently weak as a Brønsted acid to prefer the carboxyl pathway (Scheme 1a). On the other hand, a decrease in selectivity towards CO (78%) and a parallel increase in H_2 production (22%) are attained in the presence of 1 M PhOH, which is consistent with the higher acidity of the proton donor and the expected favorable acceleration of a hydride pathway (Scheme 1b) in the presence of stronger acids. Thus, the analysis points out the critical role of the proton donor in dictating both the activity and the selectivity of **FeL^{MeOH}** towards the CO_2RR, with TFE representing the optimal proton source to achieve stable catalysis and high selectivity for the formation of CO.

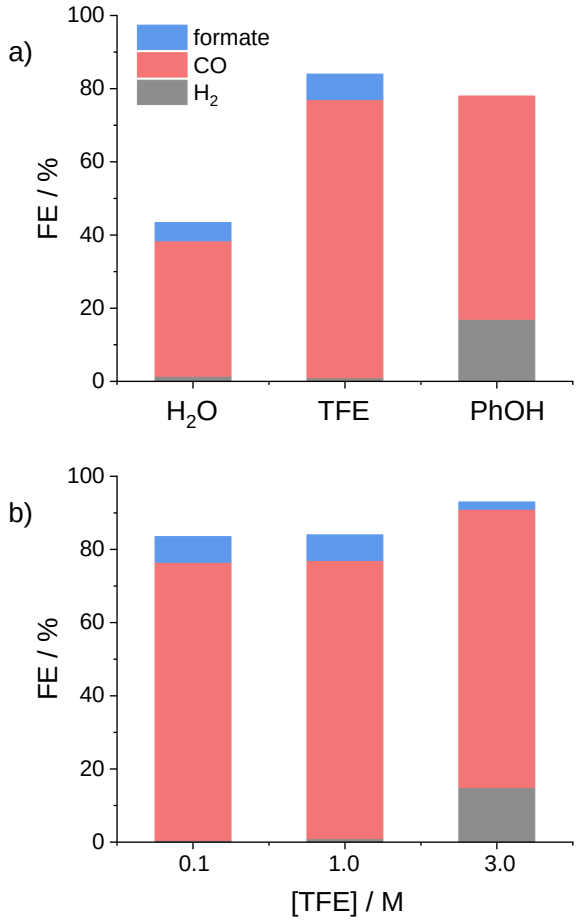

Figure 2. Faradaic efficiencies (FE) of product formation after 2 h CPE at −2.0 V vs Fc^+/Fc of 1 mM complex **FeL^{MeOH}** in CO_2-saturated acetonitrile in the presence of a) 1 M proton donor and b) variable concentrations of TFE.

It should be also noticed that with both H_2O and TFE (Entries 1-3 and 4-6 in Table 1, respectively), increasing the proton donor concentration leads to a general increase in catalyst stability (total FE up to 82.5% and 93% with 5.5 M H_2O and 3 M TFE, respectively) and a concurrent, slight decrease in selectivity towards CO, indicating that at high concentration of H_2O and TFE the hydride pathway (Scheme 1b) starts becoming competitive. Consistent with this observation, a similar trend is also followed using PhOH as the proton donor, but only when

limiting the concentration within the 0.1-1 M range (Entries 7,8 in Table 1). An additional increase in the amount of PhOH up to 3 M leads indeed to the selective formation of hydrogen as the catalysis product (Entry 9 in Table 1). These results thus highlight the critical relationship between pK_a and concentration of the proton source to modulate product yield and selectivity.

Table 1. Summary of bulk electrolysis data of 1 mM **FeL^{MeOH}** in acetonitrile.[a]

			Faradaic Efficiency / %			**Selectivity / %** [c]		
Entry	**HA**	**[HA] / M**	**H_2**	**CO**	**Formate**	**H_2**	**CO**	**Formate**
1[b]	H_2O	0.55	0.3	34	6	0.7	84.3	15.0
2	H_2O	1.0	1.4	37	5	3.2	86.4	10.4
3[b]	H_2O	5.5	4.5	63	15	5.5	76.5	18.0
4	TFE	0.1	0.5	76	7	0.5	90.7	8.8
5	TFE	1.0	1	76	7	1.2	90.5	8.3
6	TFE	3.0	15	76	2	16.1	81.8	2.1
7	PhOH	0.1	0.6	32	2	1.7	92.5	5.8
8	PhOH	1.0	17	61	-	22	78	-
9	PhOH	3.0	50	-	-	100	-	-

[a] Estimated after 2 h, 1 mM catalyst concentration, CO_2-saturated solution, 0.1 M $TBAPF_6$, glassy carbon as working electrode, Pt as the counter electrode, SCE as the reference, applied potential of −2.0 V vs Fc^+/Fc; [b] taken from ref 37; [c] estimated as the ratio between the amount of each product and the total amount of products.

Finally, a detailed inspection of the catalytic data in Table 1 shows that at high H_2O content a larger fraction of formate than H_2 is attained (FE of 15% and 4.5% at 5.5 M H_2O, respectively), while an opposite trend is apparent using TFE (FE of 2% and 15% at 3 M TFE for formate and H_2, respectively). This can be explained considering the enhanced reactivity of the

putative Fe(II)-hydride intermediate with the proton donor (H_2 formation) over CO_2 (formate production), expected to increase with lowering the pK_a of the acid source.[50] The failure to observe formate at >1 M PhOH is also consistent with this notion.

Catalytic mechanism

The catalytic mechanism leading to the formation of CO was investigated by employing DFT-D3//COSMO-RS calculations (for details see Materials and methods). We examined the EECC pathway, which is expected to be the dominating mechanism under electrochemical conditions, according to the data reported above. The mechanistic proposal is schematically illustrated in Scheme 2, alongside with the computed energetics, which are additionally summarized in Figure 3. The first (chemical) step considered is the binding of CO_2 to the two-electron reduced catalyst. It is computed to be endergonic by 13.3 kcal·mol^{-1} with an activation barrier of 16.6 kcal·mol^{-1}. Thus, it most likely represents the rate determining step of the catalytic reaction as experimentally envisioned (*vide supra*). The next step is the protonation of the ensuing iron carboxylate adduct. Due to the low proticity of the solution, the number of dissolved protons in the reaction medium is negligible and thus this reaction step should be interpreted as an intermolecular PT, i.e., the proton is expected to come from an acid (here H_2O, TFE, or PhOH) and not bulk solution. The calculated pK_a value of [LFe-COOH]$^+$ (25.9) is comparable but slightly lower than that of PhOH, thus the PT is endergonic when TFE or H_2O are used as proton donors. This provides a potential explanation for the observed improvement of the reaction kinetics with increasing pK_a and concentration of the proton donor. The third step is an intermolecular PT to the previously formed carboxyl moiety, followed by a dehydration reaction. Unfortunately, under the employed methodology, the activation barrier of the

dehydration reaction cannot be determined, as water spontaneously detaches from the complex during even conservative geometry optimization procedures and engages in an intramolecular PT when the C-O distance is constrained, indicating another negligible barrier. For this reason, thermodynamic information is provided only for the combination of protonation and dehydration. This combined step is highly exergonic by –29.6 kcal·mol^{-1} (Scheme 2), consistent with a much faster reaction than in the previous steps. The last step in the catalytic cycle is the detachment of CO from the catalyst or, alternatively, its replacement by a solvent molecule. For the former process, DFT predicts ΔG = –8.8 kcal·mol^{-1} and an activation barrier of only $\Delta G^{\ddagger}$ = 0.6 kcal·mol^{-1}, suggesting favorable and rapid removal of CO, and recovery of the starting Fe(II) catalyst. The predicted rapid removal of CO might pose an essential design feature of the catalytic system, as it prevents the formation of more stable metal carbonyls by additional electronic reductions. The thermodynamic feasibility of this reaction step is also corroborated by the experimental finding that bubbling of CO into an acetonitrile solution of **FeL$^{\mathbf{MeOH}}$** does not lead to formation of the corresponding carbonyl complex.[49]

Scheme 2. Proposed EECC reaction mechanism for the CO formation by **FeL$^{\mathbf{MeOH}}$** in acetonitrile calculated at the B3LYP-D3(BJ)/ COSMO-RS/def2-TZVPD level of theory. All computed free energies and the activation energies are given in kcal·mol^{-1}, reduction potentials in V. Identifiers: starting point (green), intermediates without ligand protonation (black), intermediates with protonation of the selected bipyridine (blue) or pyridine (red). The superscript preceding the identifier of the complex denotes the spin-state. Note that the dehydration step designated with the asterisk (*) assumes the presence of free protons, making its comparability dependent on the calculated pK_a value of the employed proton donor (see Table S1). The $\Delta G^{\ddagger}$

designated with two asterisks (**) refers to the simple elimination of CO without solvent binding.

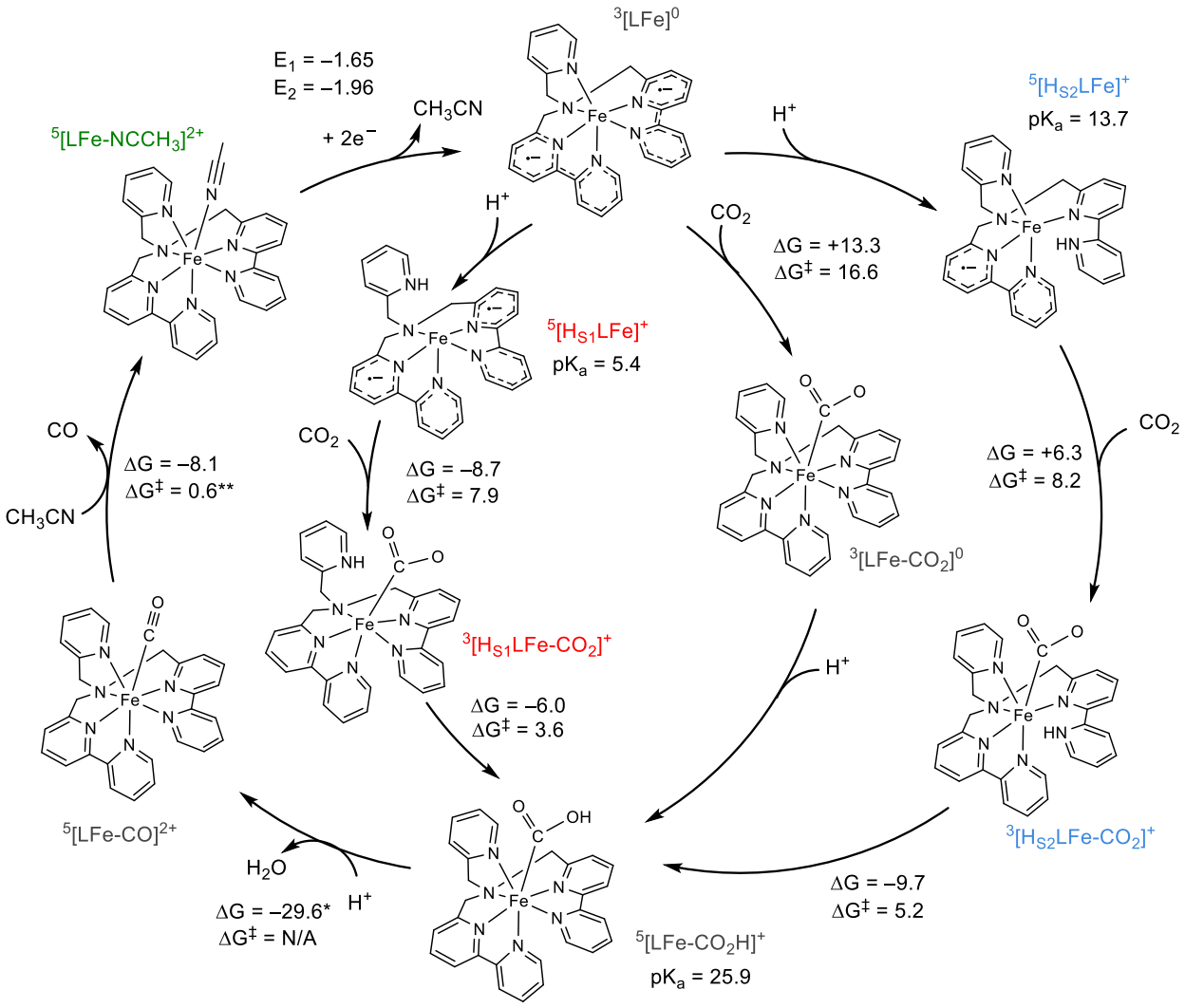

Protonation of the DBPy-PyA ligand after the second reduction step was also considered in the reaction mechanism as it has the potential to alter the reaction cycle (Scheme 2). Here, we only consider protonation of the pyridine moiety and of the distal pyridine ring (farther from amine moiety) of the bipyridine moiety neighboring the solvent ligand coordination site. We mainly justify this limitation with the inability of the proximal pyridine rings of the bipyridine moieties (i.e., those closer to the tertiary amine) to form stable conformers without the breaking

of additional metal-ligand bonds. Detachment of the pyridine experiences a lower activation barrier (11.4 kcal·mol^{-1}) than the detachment of bipyridine (18.6 kcal·mol^{-1}). However, both barriers are reasonably low and thus the ensuing protonation process is mainly expected to be thermodynamically, rather than kinetically driven. Calculated pK_a values of the protonated DBPy-PyA ligand and binding free energies are summarized in Scheme 2. They indicate that the protonation of the pyridine moiety is less favored and can be reasonably disregarded under the employed experimental conditions. Protonation of the bipyridine moiety is instead more likely and has a considerable stabilizing and accelerating effect on the binding of CO_2, likely resulting from the reduction of the steric hindrance due to the freed-up coordination side. Computational data further indicate that, after the binding of CO_2 to the catalyst, an intramolecular PT from the protonated DBPy-PyA ligand to the CO_2 moiety is highly favorable from a thermodynamic standpoint. This highlights the role of the hexadentate ligand in actively assisting PT events in catalysis by functioning as a proton reservoir.[28,29,31]

Formation of CO by **FeL^{MeOH}** is observed to compete with hydrogen and/or formate generation. The primary step in both cases is the formation of a metal-hydride bond by direct PT to the metal center of the two-electron-reduced catalyst (Scheme 3). The propensity of the catalyst to form the hydride species is indeed equally important as the binding of CO_2 in dictating the selectivity of the catalytic process. Calculated pK_a values indicate that protonation of the metal center is thermodynamically comparable to protonation of the selected bipyridine moiety of the DBPy-PyA ligand (Scheme 3). The hydride species can trigger HER via different reaction pathways. First, the evolution of hydrogen can occur by direct abstraction of a proton from a dissolved acid by the hydride. Another plausible pathway involves the protonation of the

Scheme 3. Proposed EECC reaction mechanism for the HER by **FeL^{MeOH}** in acetonitrile. All Δ*G* values are displayed in kcal·mol^{-1}, calculated at the B3LYP-D3(BJ)/COSMO-RS/def2-TZVPD level of theory. Identifiers: starting point (green), intermediates without ligand protonation (black), intermediates with protonation of the selected bipyridine (blue) or pyridine (red). The superscript preceding the identifier of the complex denotes the spin-state. Whenever two deprotonations are specified, p$K_{a,1}$ and p$K_{a,2}$ refers to the deprotonation of the metal center and DBPy-PyA ligand, respectively. Note that the evolution of H_2 in the step designated with the asterisk (*) assumes the presence of free protons, making its comparability to the other displayed mechanisms dependent on the calculated pK_a value of the employed proton donor (see Table S1).

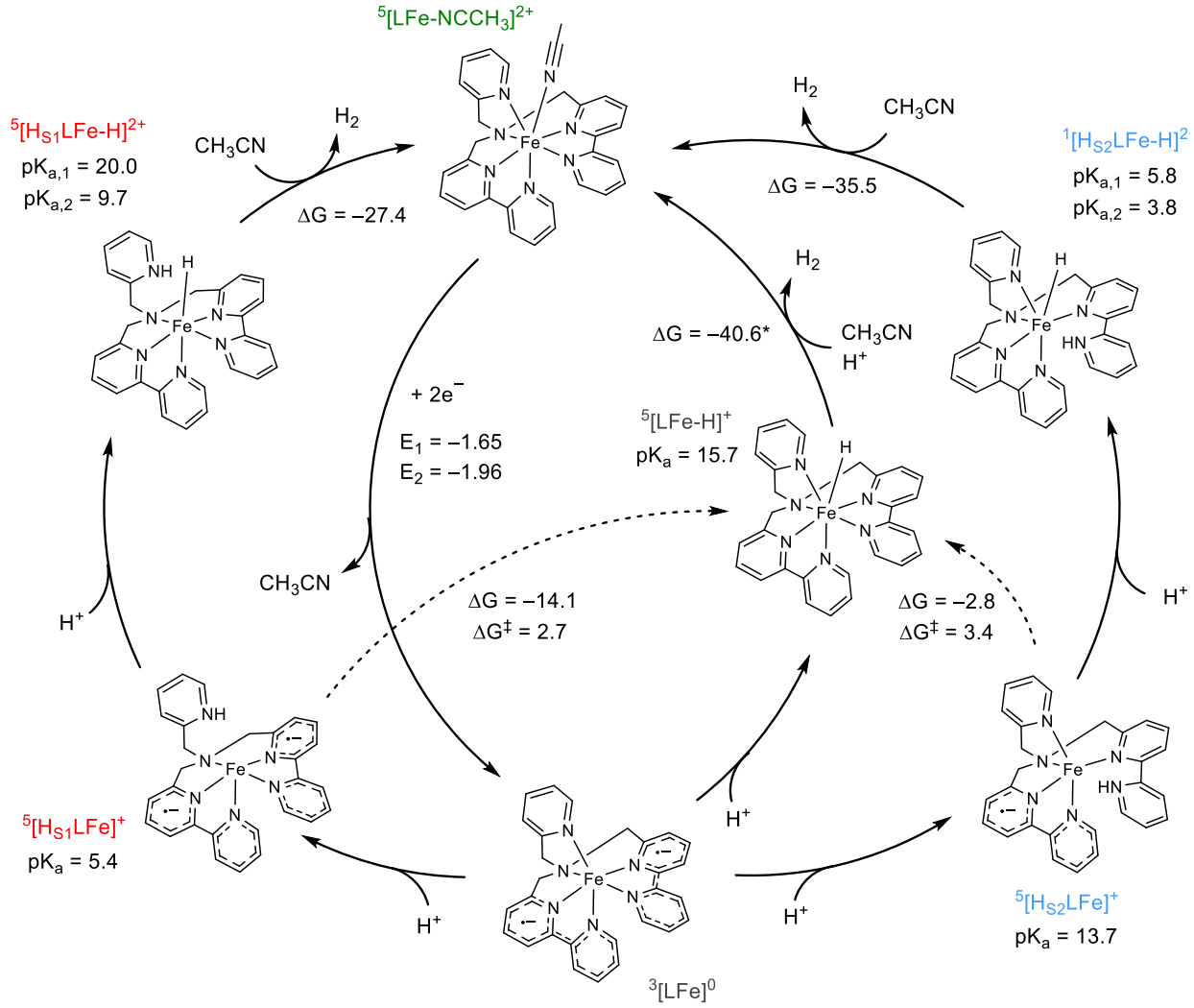

DBPy-PyA ligand followed by an intramolecular PT to the hydride, leading to the evolution of H_2.[51] Formation of formate, on the other hand, can be attained by the direct transfer of the hydride to a dissolved CO_2 molecule. Notably, the protonation of the two-electron reduced complex is thermodynamically less favorable than CO_2 binding (see, e.g., the energy profile in Figure 3 using TFE as the proton donor). Furthermore, protonation of the DBPy-PyA ligand significantly reduces the propensity for the protonation of the reduced metal center. Under these circumstances, CO_2 binding would result more favorable, thereby explaining the more pronounced tendency of **FeL^{MeOH}** to follow the carboxyl pathway leading to the selective formation of CO.

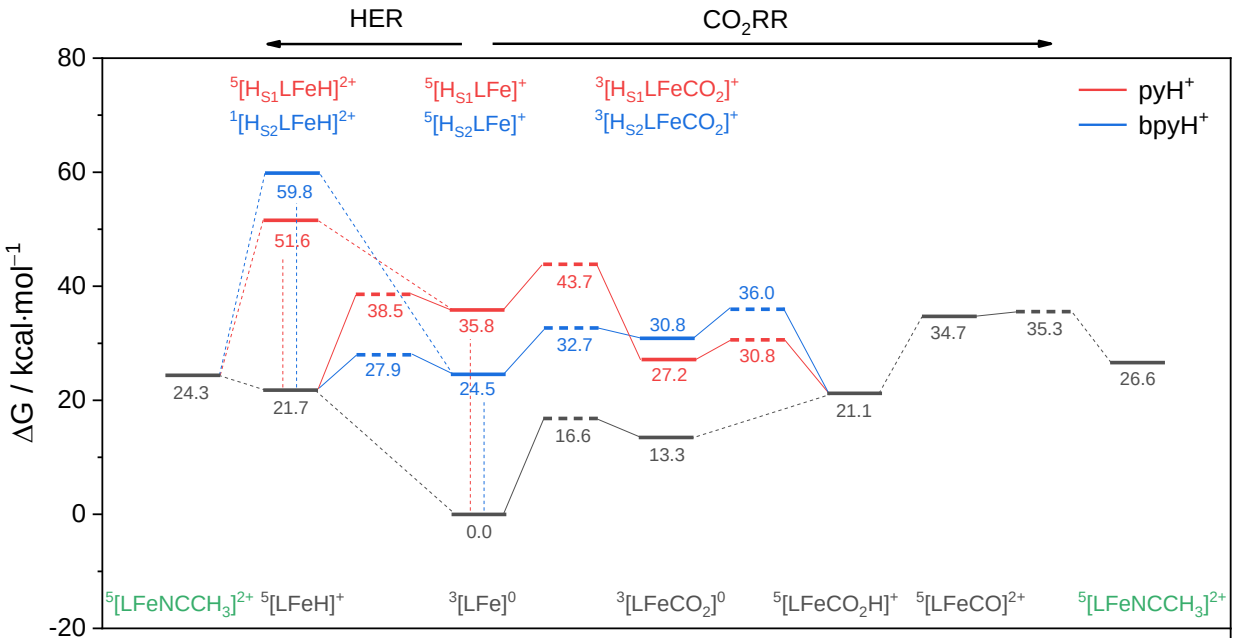

Figure 3. Gibbs free energy profile of the CO_2RR and HER without ligand protonation (black), and with protonation of the selected bipyridine (blue) or pyridine (red) of the DBPy-PyA ligand. Free energies of intermolecular PTs to the catalyst are given in reference to TFE. Intermediate products are marked by solid bars and transition states are denoted by dashed horizontal lines, dashed connecting lines indicate that a transition state for the process cannot be determined.

Photochemical CO_2 reduction

The catalytic activity of **FeL^{MeOH}** in CO_2-saturated acetonitrile was further examined and optimized within the light-activated cycle involving $[Ru(bpy)_3]^{2+}$ as the sensitizer and DIPEA as the sacrificial electron donor under 1 sun (0.1 $W \cdot cm^{-2}$) irradiation. Figure 4 depicts the most relevant results (see Figures S29-S43 for the remaining kinetics), while the photochemical data in terms of maximum amount of photoproduct, turnover number (TON), selectivity, turnover frequency (TOF), and quantum yield (Φ) are collected in Table 2. For a better comparison with literature data, we have now estimated the quantum yield of CO formation, defined as the ratio between the moles of CO product and the absorbed photons, via actinometry (see Supporting Information for details).[52] We should consider that while the amount of gaseous products is strongly dependent on the experimental conditions, a similar quantity of formate (< 4 μmol) is always found, in line with that attained in control experiments without **FeL^{MeOH}** (Table S6). As already reported,[53] this quantity most likely originates from the parallel degradation of the sensitizer and the concurrent formation of ruthenium-based molecular species, whose catalytic activity results in the preferential formation of formate. Thus, differently from what observed in the electrochemical tests, we reason that under light-driven conditions only minor, if any, generation of formate occurs through direct catalysis by the iron complex. Similar findings were reported by Fujita and co-workers when comparing the electrochemical and photochemical activity of a polypyridine cobalt complex,[54] which was ascribed to the parallel formation of additional acid sources upon decomposition of the electron donor,[60] which could impact on the overall product yield. According to these considerations, for the sake of simplicity, the data collection (Table 2) and the following discussion have been limited to the CO and H_2 products.

We first started from the conditions employed in our previous work, i.e., using H_2O as the proton adjutant, and studied the effect of the concentration of both the proton donor and the catalyst. Inspection of the catalytic data shows that at a fixed concentration of **FeL^{MeOH}** (50 μM) the selectivity towards the formation of CO is generally high (>92%) and weakly influenced by

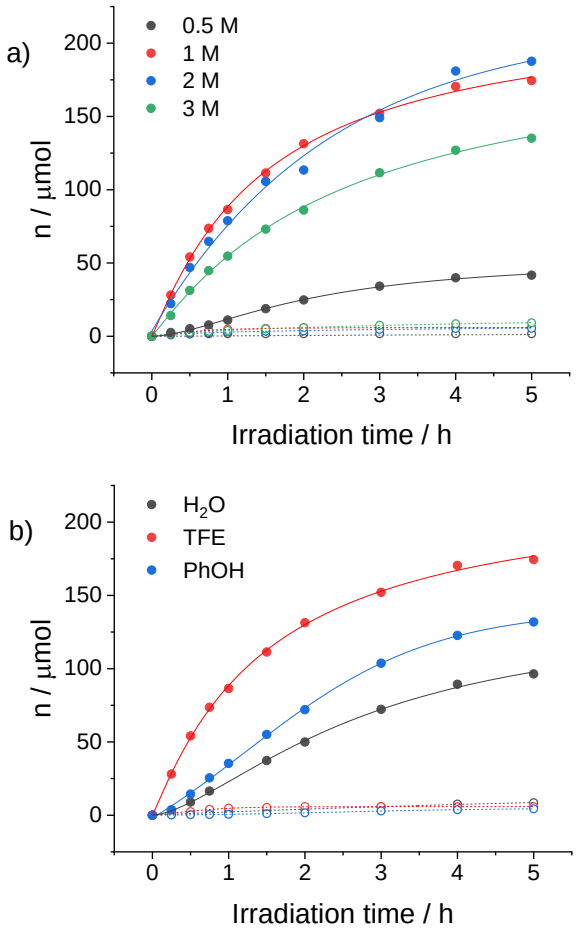

Figure 4. Kinetics of CO (full dots) and H_2 (empty dots) formation upon visible-light irradiation (400-800 nm, 1 sun) of CO_2-saturated acetonitrile solution containing 0.4 mM $[Ru(bpy)_3](PF_6)_2$, 0.1 M DIPEA, 50 μM **FeL^{MeOH}**, a) at different concentrations of TFE and b) in the presence of 1 M proton donor.

Table 2. Summary of the photochemical data.[a]

				n / μmol (TON) [c]		Selectivity / % [d]		Efficiency	
Entry	**[Fe] / μM**	**HA**	**[HA] / M**	**H_2**	**CO**	**H_2**	**CO**	**TOF_{CO} / h^{-1}**	**Φ_{CO} / % [e]**
1[b]	50	H_2O	0.55	2.4 (9)	43.3 (173)	5	95	66	1.5
2	50	H_2O	1	8.4 (34)	96.3 (385)	8	92	103	2.5
3[b]	50	H_2O	5.5	2.7 (11)	44.0 (176)	6	94	98	2.4
4[b]	10	H_2O	5.5	9.0 (180)	18.6 (372)	33	67	240	1.1
5	5	H_2O	5.5	2.6 (104)	7.0 (278)	27	73	98	0.3
6	2	H_2O	5.5	1.0 (102)	3.1 (305)	24	76	144	0.1
7	50	TFE	0.5	1.7 (7)	41.6 (166)	4	96	51	1.3
8	50	TFE	1	5.8 (23)	174.5 (698)	3	97	394	9.4
9	50	TFE	2	5.5 (22)	187.6 (750)	3	97	360	8.6
10	50	TFE	3	9.2 (37)	135.1 (540)	6	94	241	5.7
11	25	TFE	1	3.1 (20)	47.1 (376)	5	95	129	1.5
12	10	TFE	1	1.9 (38)	17.0 (340)	10	90	96	0.4
13	2	TFE	1	1.1 (110)	3.5 (350)	24	76	138	0.1
14	50	PhOH	0.5	1.1 (4)	90.7 (363)	1	99	115	2.8
15	50	PhOH	1	4.3 (17)	131.8 (527)	3	97	168	4.0
16	50	PhOH	3	44.7 (179)	12.2 (49)	78	22	28	0.7
17	10	PhOH	1	8.0 (160)	122.1 (2442)	6	94	768	3.6
18	2	PhOH	1	3.6 (363)	19.7 (1972)	15	85	491	0.4

[a] Visible-light irradiation (400-800 nm, 1 sun), 0.4 mM $[Ru(bpy)_3](PF_6)_2$, 0.1 M DIPEA in acetonitrile; [b] taken from ref 37; [c] estimated after 5 h irradiation; [d] estimated as the ratio between the amount of a single product and the total amount of products; [e] calculated using actinometry (see Supporting Information).

the H_2O content (Entries 1-3 in Table 2). Interestingly, an increase in the amount of H_2O from 0.55 to 1 M results in an improvement of the performance in terms of both efficiency and amount of CO product. However, a further increase in the concentration of H_2O up to 5.5 M does not lead to additional enhancements in activity. On the other hand, at 5.5 M H_2O, decreasing the catalyst concentration (Entries 3-6 in Table 2) is accompanied by a general lowering of both the activity (amount of gaseous products and quantum yield) and selectivity towards CO. This possibly indicates that, under these conditions, catalyst reduction by the photogenerated $[Ru(bpy)_3]^{2+}$ species might limit the light-driven catalytic activity.

We then moved to test TFE as the proton donor and checked similarly the effect of its concentration (Figure 4a and Entries 7-10 in Table 2). Akin to water, a similar bell-shaped trend is apparent, with the performances, both in terms of amount and rate of CO production, peaking for intermediate concentrations (1-2 M). More importantly, with TFE as the proton donor a net improvement with respect to H_2O is observed at 50 μM catalyst loading in terms of both activity and selectivity. A maximum amount of 187.6 μmol of CO product with a selectivity of up to 97%, corresponding to a maximum TON of 750, and a quantum yield of CO formation of 9.4% are indeed attained using TFE (Table 2), paralleling the gain in catalytic performances already recorded in electrochemical experiments (Figure 4b). Although the maximum TON is not particularly large, due to the use of a 50 μM concentration of catalyst,[55] the amount of CO formed under these conditions corresponds to 0.85 mL of product per mL of solution and is, to the best of our knowledge, one of the largest attained in light-driven CO_2 reduction with molecular sensitizers and catalysts. Similar (but lower) CO amounts were obtained recently by Chang and co-workers using a polypyridine iron complex with $[Ru(bpy)_3]^{2+}$ (ca 160 μmol per 5 mL photolyzed solution)[10] and by Ouyang and co-workers, using a cobalt(II) catalysts and a

copper(I) sensitizer (135-140 μmol per 4 mL).[56,57] Similar values were only recorded by Robert and co-workers using a cobalt polypyridine complex and an organic dye (95 μmol per 2.5 mL photolyzed solution),[58] but after a much longer irradiation period (24 h). For **FeL^{MeOH}**, akin to what was observed using H_2O as the proton donor, lowering the catalyst concentration down to 2 μM at a constant TFE concentration (1 M) leads to a progressive diminishment of the activity and selectivity for CO formation (Entries 11-13 in Table 2), still suggesting a kinetically limiting catalyst activation step.

Replacing the TFE proton donor with the more acidic PhOH does not lead to an improvement in catalytic activity in terms of both maximum amount of CO product and quantum yield, with the best results attained at 1 M PhOH. Notably, a remarkably high selectivity of 99% towards CO formation is achieved at 50 μM catalyst and 0.5 M PhOH (Entry 14 in Table 2). On the other hand, increasing the concentration of this proton donor up to 3 M (Entries 15,16 in Table 2) leads to a complete reversal in the major catalytic product (selectivity of only 22% for CO). Interestingly, decreasing the catalyst concentration at 1 M PhOH (Entries 16-18 in Table 2) results in a less pronounced abatement of the catalytic activity than observed with both H_2O and TFE proton donors. This can be likely explained assuming an acceleration of the chemical steps within the EECC catalytic mechanism using the more acidic PhOH, possibly leading to faster catalyst turnover under light-driven conditions and reduced decomposition routes involving the sensitizer (see below). Although lower amounts of CO product (at correspondingly lower rates and efficiencies) are attained at low catalyst loadings, a gain in terms of both maximum TON and TOF can be recorded at 10 μM catalyst concentration with values up to 2442 and 768 h^{-1}, respectively.

Control experiments in the absence of the electron donor, the sensitizer, or light do not yield detectable photoproducts (Entries 1-3 in Table S6 of the Supporting Information), whereas small amounts of CO, H_2 and formate are detected in the absence of the iron catalyst (Entries 5-7 in Table S6). CO was also attained at 50 μM **FeL^{MeOH}** in the absence of any proton donor, but in lower yield (Entry 8 in Table S6), confirming the relevant role of the acid source in accelerating catalysis. Importantly, when photochemical catalysis was attempted in the absence of CO_2 (using Ar as an inert gas), only traces of H_2 were detected (Entry 4 in Table S6), thus demonstrating that the formed CO clearly originates from catalytic conversion of CO_2 by the iron complex. Overall, the control experiments confirm that the added components (sensitizer, catalyst, electron and proton donors) and light are all required to achieve sustained CO formation from CO_2.

After the investigation and optimization of the light-driven experiments, we next turned to the experimental conditions that provided the largest amount of CO product with the highest quantum yield, namely 50 μM **FeL^{MeOH}** and 1 M TFE (Entry 8 in Table 2), to examine the turnover limiting factors of the photochemical system. We first hypothesized that a possible reason for the levelling-off of the light-driven activity could be the consumption of the reactants required to promote the catalytic generation of CO, namely the CO_2 substrate, the TFE proton donor, and the DIPEA electron donor. At 1 M TFE, a maximum amount of 175 μmol of CO product is formed, which corresponds to an overall consumption of 12.5%, 7%, and 35% of the initial quantities of CO_2, TFE and DIPEA, respectively. In this regard, particularly critical is the decrease of the DIPEA concentration which might impact on the efficiency of the primary photochemical reaction considering the slow bimolecular rate constant for the reductive quenching of the excited sensitizer ($k = 6.6 \cdot 10^6$ $M^{-1}s^{-1}$).[37] Consistent with this hypothesis, after 2 h irradiation (Figure 5a), purging of the photolyzed solution with CO_2 and concomitant addition

of the required amounts of both TFE and DIPEA to restore their corresponding initial concentrations (1 and 0.1 M, respectively) leads to a partial recovery of the light-driven catalytic activity (ca 45% in terms of total moles of CO with respect to the quantity produced after 2 h).

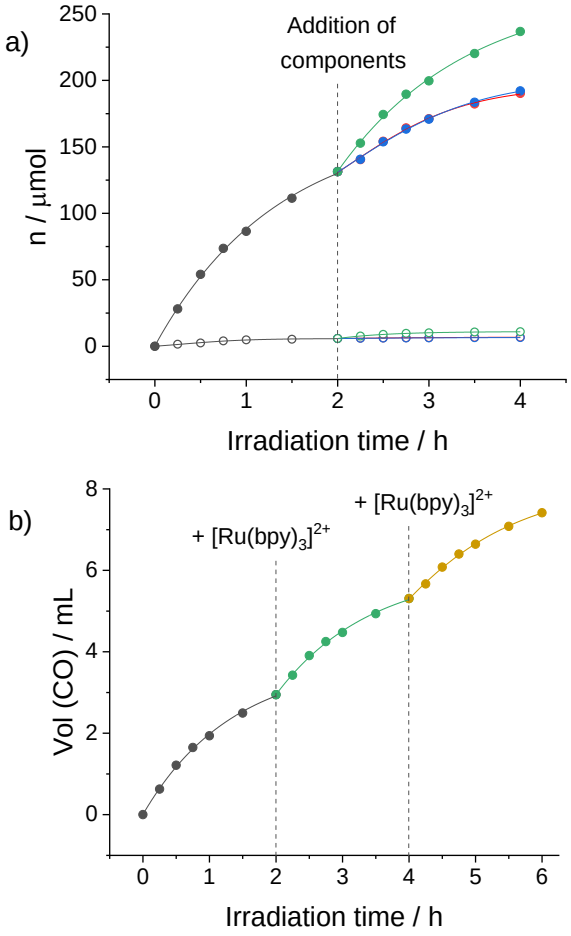

Figure 5. a) Effect of the addition of CO_2, DIPEA, TFE (red), CO_2, DIPEA, TFE and **FeL^{MeOH}** (blue), and CO_2, DIPEA, TFE and $[Ru(bpy)_3](PF_6)_2$ (green) on the kinetics of CO (full dots) and H_2 (empty dots) formation upon visible-light irradiation (400-800 nm, 1 sun) of acetonitrile solution containing 0.4 mM $[Ru(bpy)_3](PF_6)_2$, 0.1 M DIPEA, 50 µM **FeL^{MeOH}**, and 1 M TFE; b) multiple light-driven cycles upon addition of CO_2, DIPEA, TFE and $[Ru(bpy)_3](PF_6)_2$ every 2 h.

Interestingly, a similar resumption is also attained upon addition of 50 μM **FeL^{MeOH}** complex together with TFE, DIPEA and CO_2, suggesting that decomposition of the catalyst does not represent a turnover limiting factor. Instead, addition of 0.4 mM $[Ru(bpy)_3](PF_6)_2$ together with TFE, DIPEA and CO_2 enables the photochemical system to restart with similar rates as those measured at the beginning of the experiment, thus confirming that progressive degradation of the sensitizer mainly limits the light-driven catalytic activity. This is indeed not unexpected for photochemical systems involving $[Ru(bpy)_3]^{2+}$ as the chromophore, due to the documented reactivity under photolysis conditions.[59] This evidence was further confirmed by the comparison of the absorption spectra before/after light-driven catalysis that shows a partial abatement of the metal-to-ligand charge-transfer (MLCT) transition characteristic of the ruthenium(II) complex (Figure S44-S46). Notably, multiple additions of the $[Ru(bpy)_3](PF_6)_2$ sensitizer every 2 h (together with TFE, DIPEA and CO_2) allow us to achieve sustained and stable CO generation upon visible-light irradiation, with quantities up to ca 8 mL after only 6 h (Figure 5b).

Mechanistic insight into photochemical CO_2 reduction

Light-driven CO_2 reduction by complex **FeL^{MeOH}** in combination with $[Ru(bpy)_3]^{2+}$ as the sensitizer and DIPEA as the sacrificial electron donor occurs through a reaction sequence involving excitation of the sensitizer (eq 1), reductive quenching of the excited state by the DIPEA (eq 2), and subsequent electron transfer from the reduced chromophore to the catalyst (eq 3), either in its initial or one-electron reduced species. Once the Fe(0) species has formed, the subsequent chemical steps, according to the reaction mechanisms depicted in Scheme 2 (or 3), are expected to lead to CO (or H_2) formation. On the other hand, the oxidized donor ($DIPEA^{\bullet+}$) undergoes deprotonation (eq 4), with the resulting radical species leading to reduction of a

ground-state sensitizer molecule (eq 5).[60] We should consider that, in principle, the latter radical may also participate in direct reduction of the **FeL^{MeOH}** complex (eq 6), although the mutual concentrations of sensitizer and catalyst are such that the reaction with the former is intrinsically more likely. According to the reaction scheme in eqs 1-6, one photon is required to attain one molecule of product (either CO or H_2).

$$[Ru(bpy)_3]^{2+} + h\nu \rightarrow {}^*[Ru(bpy)_3]^{2+} \quad (1)$$

$${}^*[Ru(bpy)_3]^{2+} + DIPEA \rightarrow [Ru(bpy)_3]^{+} + DIPEA^{\bullet+} \quad (2)$$

$$[Ru(bpy)_3]^{+} + C_{ox} \rightarrow [Ru(bpy)_3]^{2+} + C_{red} \quad (3)$$

$$DIPEA^{\bullet+} + DIPEA \rightarrow DIPEA^{\bullet} + DIPEAH^{+} \quad (4)$$

$$[Ru(bpy)_3]^{2+} + DIPEA^{\bullet} \rightarrow [Ru(bpy)_3]^{+} + \textit{degradation products} \quad (5)$$

$$DIPEA^{\bullet} + C_{ox} \rightarrow C_{red} + \textit{degradation products} \quad (6)$$

Transient absorption spectroscopy was employed to follow the proposed reaction sequence and to attain kinetic insight into the relevant electron transfer steps. Pulsed excitation at 532 nm of an acetonitrile solution containing 70 μM $[Ru(bpy)_3]^{2+}$, 0.1 M DIPEA and 0.25 mM **FeL^{MeOH}** leads to the formation of a transient spectrum at 0.1 μs time-delay (Figure 6a) featuring a positive absorption at 370 nm, a negative absorption at 450 nm due to depletion of the MLCT transition, and an apparent bleaching at 620 nm due to spontaneous emission. These fingerprints are characteristic of the triplet excited state of the $[Ru(bpy)_3]^{2+}$ chromophore.[61] A spectral evolution is first observed within ca 2 μs (Figure 6a), showing a partial decrease of both the positive and negative absorptions associated with the excited state and the concurrent formation of a new positive absorption at 505 nm. The latter is the peculiar absorption expected for the formation of

the reduced sensitizer $[Ru(bpy)_3]^+$ and the spectral changes can thus be assigned to the reductive electron transfer process between the excited state of the $[Ru(bpy)_3]^{2+}$ chromophore and the DIPEA donor (eq 2).[61] Kinetic analysis (Figure 6c and Figures S47, S48) yields an average time-constant of ca 670 ns for this process, which is in good agreement with the decay rate of the $*[Ru(bpy)_3]^{2+}$ excited state in the presence of 0.1 M DIPEA, estimated considering the bimolecular rate constant of $k = 6.6 \cdot 10^6$ $M^{-1}s^{-1}$ for the electron transfer process in eq 2.[37] The subsequent spectral evolution was then monitored within the 2-1000 μs timeframe (Figure 6b), which is characterized by the progressive decrease of both absorption at 355 and 500 nm and the parallel formation of a broad absorption throughout the whole spectrum (isosbestic points at 387, 470, and 565 nm). This process can be assigned to the reduction of catalyst **FeL^{MeOH}** by the photogenerated $[Ru(bpy)_3]^+$ sensitizer (eq 3, where C_{ox} and C_{red} are the Fe(II) and Fe(I) species, respectively). Formation of a broad absorption in the red portion of the visible spectrum is indeed expected for the reduction of the iron complex.[37] Kinetic analysis of the $[Ru(bpy)_3]^+$ decay (Figure 6c and Figure S47) or Fe(I) formation (Figure S48) gives a time-constant of ca 50 μs for the electron transfer process in eq 3. Considering the higher concentration of **FeL^{MeOH}** complex (0.25 mM) than the photogenerated $[Ru(bpy)_3]^+$ sensitizer (ca 9 μM, according to the Lambert-Beer law considering a $\Delta\varepsilon = 9000$ $M^{-1}cm^{-1}$ at 500 nm and the actual optical pathlength)[62] and the resulting pseudo-first order conditions, a bimolecular rate constant of $k = 8 \cdot 10^7$ $M^{-1}s^{-1}$ can be extracted for this electron transfer reaction. Interestingly, this value is considerably lower than that found in analog cobalt polypyridine complexes for which the bimolecular rate constants typically approach the diffusion-controlled regime.[22,28,29,31] This evidence is indeed not fully unexpected considering the small driving force for Fe(II)→Fe(I) reduction by $[Ru(bpy)_3]^+$ ($\Delta G = -0.11$ eV, taking $E = -1.76$ V vs Fc^+/Fc for the $[Ru(bpy)_3]^{2+}/[Ru(bpy)_3]^+$ couple[63] and neglecting

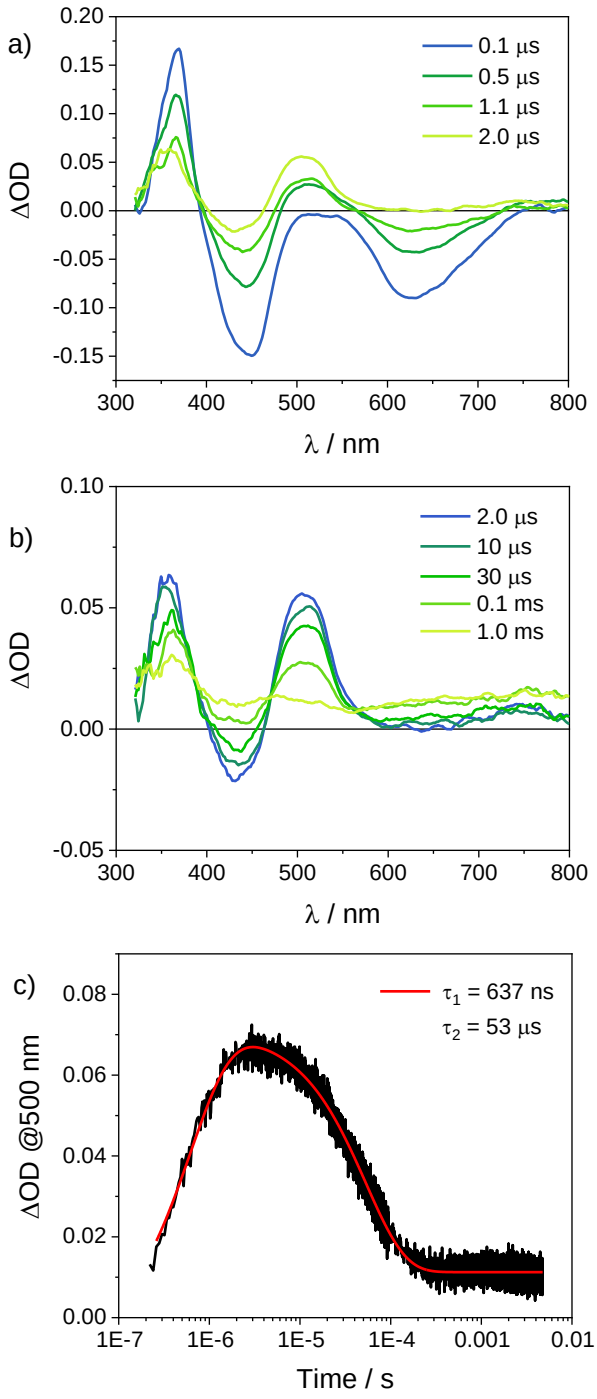

Figure 6. Spectral changes between a) 0.1-2 µs and b) 2-1000 µs and c) kinetic analysis at 500 nm obtained by laser flash photolysis (excitation at 532 nm) of an acetonitrile solution containing 70 µM $[Ru(bpy)_3]^{2+}$, 0.1 M DIPEA and 0.25 mM **FeL^{MeOH}** under N_2.

electrostatic work terms). Furthermore, it also suggests that the subsequent Fe(I)→Fe(0) reduction might be still slower, based upon the slight endergonicity of the process (ΔG = +0.09 eV, neglecting electrostatic work terms).

The results obtained by laser flash photolysis indicate that catalyst activation by the photogenerated $[Ru(bpy)_3]^+$ could potentially represent the rate-determining step in light-driven catalysis within the **FeL^{MeOH}**/$[Ru(bpy)_3]^{2+}$/DIPEA three-component system. Within this assumption, we reasoned that the observed instability of the $[Ru(bpy)_3]^{2+}$ chromophore, which represents the turnover-limiting factor in our light-driven catalytic tests, mainly arises from parallel decomposition routes involving the photogenerated $[Ru(bpy)_3]^+$ species. As a matter of fact, in the absence of an efficient electron collection by the **FeL^{MeOH}** catalyst, its accumulation upon prolonged photolysis may lead to unwanted, detrimental reaction pathways[59] possibly impacting on the quantum efficiency of the light-driven reaction. Starting from this hypothesis, we turned our attention to the possibility of limiting the generation of reduced $[Ru(bpy)_3]^+$ species by playing on the photon flux that reach the photochemical reactor. In Figure 7a it is reported a comparison of the kinetic traces of CO formation from a CO_2-saturated acetonitrile solution containing 0.4 mM $[Ru(bpy)_3](PF_6)_2$, 0.1 M DIPEA, 50 μM **FeL^{MeOH}**, and 1 M TFE upon irradiation with either the Xe lamp at 1 sun (black trace) or with a 460-nm LED at variable applied potentials (red and blue traces), corresponding to progressively decreasing absorbed photon fluxes. Interestingly, while the maximum amount of CO product formed is similar and the rate of CO generation slightly increases only at an intermediate photon flux (Figure 7a), calculation of the quantum yield of CO formation shows a dramatic improvement, reaching an impressive value of 28% at low power irradiance (Figure 7b). More in details, the quantum yield of CO formation can be described according to eq 7, where η_{photo} and η_{dark} are the efficiencies of

the photogeneration of the reduced $[Ru(bpy)_3]^+$ species (photochemical step) and of the dark, catalytic process (dark step), respectively. The efficiency of the photochemical step (η_{photo}) can be calculated from eq 8, knowing the quenching yield of the excited state of the $[Ru(bpy)_3]^{2+}$ chromophore by 0.1 M DIPEA ($\eta_q \sim 34\%$) and the cage escape yield associated with $[Ru(bpy)_3]^+$ formation ($\eta_{ce} \sim 100\%$, as estimated from the transient absorption spectra in Figure 6a).[64]

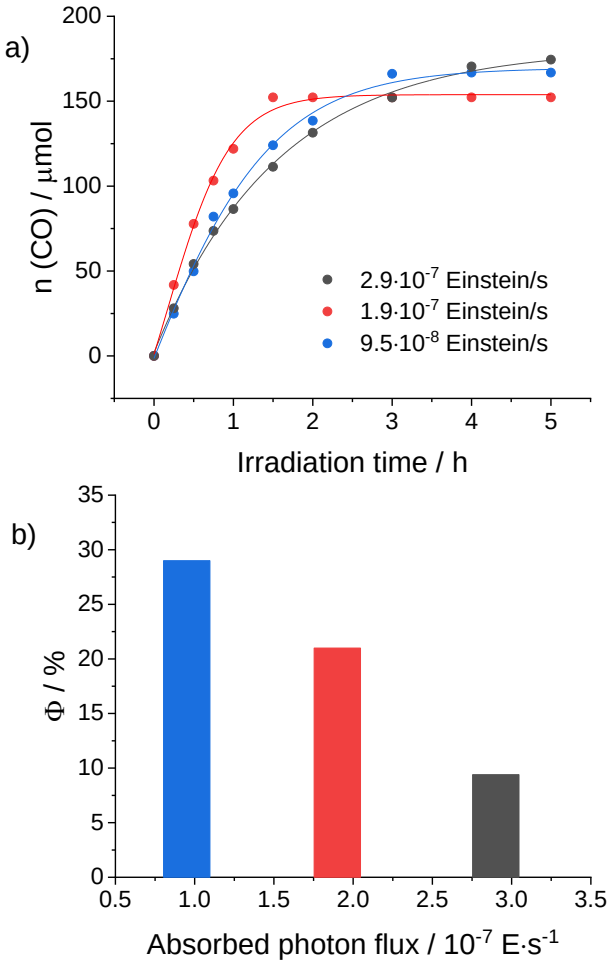

Figure 7. a) Kinetics of CO formation upon irradiation of CO_2-saturated acetonitrile solution containing 0.4 mM $[Ru(bpy)_3](PF_6)_2$, 0.1 M DIPEA, 50 µM **FeL^{MeOH}**, and 1 M TFE at different absorbed photon fluxes attained using either the Xe lamp (black) or a 460-nm LED (red, blue); b) trend of the quantum yield vs. absorbed photon flux.

$$\Phi = \eta_{photo} \cdot \eta_{dark} \quad (7)$$

$$\eta_{photo} = 2 \cdot \eta_{q} \cdot \eta_{ce} \quad (8)$$

From these data, an almost three-fold improvement from η_{dark} ~ 14% under 1 sun irradiation up to η_{dark} ~ 41% under low irradiance conditions (i.e., 460-nm LED at $9.5 \cdot 10^{-8}$ Einstein/s) can be attained in the efficiency of the dark catalytic process. These findings point out the great potential of tuning the irradiation source towards the optimization of the catalytic reaction under light-activated conditions. Similar evidences were also documented for water oxidation catalysis[65-68] and highlight how photon management can be profitably exploited to improve the efficiency in terms of photon-to-product conversion. Furthermore, these results well comply with recent reports on more general photocatalytic reactions,[69-71] showing how modulation of the light source can have a profound impact on the performances of photochemical systems.

MATERIALS AND METHODS

Experimental Section. All reagents were obtained from standard suppliers and used without additional purification. Complex **FeL$^{\mathbf{MeOH}}$** was synthesized following literature protocols.[37] $[Ru(bpy)_3]PF_6$ was obtained by salt metathesis from the $[Ru(bpy)_3]Cl_2 \cdot 6H_2O$. Absorption spectra were recorded at room temperature using an Agilent Technologies spectrophotometer. Transient absorption spectroscopy measurements were conducted using a custom laser spectrometer comprising of a Continuum Surelite II Nd: YAG laser (FWHM = 8 ns) with frequency doubled option (532 nm). Photomultiplier signals (kinetic traces) were processed using a Teledyne

LeCroy 604Zi (400 MHz, 20 GS/s) digital oscilloscope. Transient spectra were recorded using a PiMax CCD Camera. Cyclic voltammetry (CV) measurements were performed on a PGSTAT302N potentiostat (Autolab) in a three-electrode cell, using a glassy carbon as the working electrode, a silver wire as the quasi-reference electrode, and a Pt wire as counter electrode. $TBAPF_6$ was employed as the supporting electrolyte. Solutions were purged for 20 min with either N_2 or CO_2 before analysis. Controlled potential electrolysis (CPE) experiments were performed in a gas-tight custom-made electrochemical cell using a high-surface area glassy-carbon rod as the working electrode, a platinum wire as the counter electrode (separated from the test solution by a frit) and SCE as the reference electrode (potentials were subsequently converted vs. Fc^+/Fc for uniformity with CV experiments by subtracting 0.4 V).[72] The head-space of the cell was connected to a gas-chromatography (GC) apparatus (see below for details) for the determination and quantification of H_2 and CO. The bulk electrolysis experiments were run in duplicate, and the results reported are averages of two independent experiments. Light-driven CO_2 reduction reaction (CO_2RR) experiments were performed under continuous visible light irradiation using two different light sources: a 175 W Xenon Arc-lamp (CERAMAX PE175BFA) and a 3 W blue LED (spectrum reported in Figure S1). For the former, an incident power of 1 sun (0.1 W/cm^2) was set using a power meter. In a typical photochemical experiment, samples were prepared in 20 mL scintillation vials by mixing stock solutions of $[Ru(bpy)_3]PF_6$ and the catalysts, followed by the addition of DIPEA and proton source (H_2O, TFE or PhOH). The solution was then placed in the reactor, purged with CO_2 for 20 minutes, continuously stirred, and maintained at constant temperature of 15°C. Experiments were run in duplicate and the results are reported as the average of two independent experiments. The measuring cell (both in cases of the bulk electrolysis and or photochemical cell) is sealed during the reaction: the head

to which the cell is attached has four ports, closed with Swagelok® connections, two of them are part of a closed loop involving GC gas inlet and sample vent to analyze the headspace content without an appreciable gas consumption, and the other two are for the degassing procedure (input and output). The gas phase of the reaction vessel was analyzed on an Agilent Technologies 490 micro-GC equipped with a 5 Å molecular sieve column (10 m), a thermal conductivity detector, and using Ar as the carrier. The unused gas sample is then reintroduced in the reactor to minimize its consumption along the whole photolysis. The moles of gases were quantified through the external calibration method. In the case of H_2, this procedure was performed through a galvanostatic (typically 1 mA) electrolysis of a 0.1 M H_2SO_4 solution. A 100% faradaic efficiency was assumed leading to a linear correlation between the amount of H_2 evolved at the cathode and the electrolysis time. CO was quantified using a response factor obtained by injecting known amounts of gas in the cell and then sampling the headspace. Average errors are within ±10% for CO and ±5% for H_2. Formate was quantified using ^{1}H-NMR (δ = 8.3 ppm).[37] The electrolyzed or photolyzed solutions were brought to basic pH upon the addition of the minimum amount of NaOH and then evaporated under reduced pressure. The solid residue was then dissolved in 2 mL D_2O and sonicated for 5 min, dimethylformamide (1 μL, δ = 7.8 ppm) was then added as an internal standard and the resulting solution was filtered before entering the NMR tube.

Computational section. All Gibbs free energies *G* calculated in this work include: electronic energy, vibrational free energy, and solvation free energy (eq 9).

$$G = E_{elec} + G_{vib} + \Delta_S G \qquad (9)$$

Geometry optimizations and electronic structure calculations were performed using the Turbomole-7.7 program package.[73] Geometry optimizations were performed at the BP86-

D3(BJ)/def2-TZVP level of theory,[74-82] and electronic structure calculations at the B3LYP-D3(BJ)/def2-TZVPD[74-78,80-84] (or ωB97M-V/def2-TZVPD[85,86] if explicitly stated) level of theory. Vibrational frequencies were calculated with Turbomole-7.7 using *in vacuo* optimized structures on the same level of theory utilized in the geometry optimization. They were converted into vibrational free energies at T = 298.15 K using the *thermo* submodule of the XTB software package[87] with an empirical scaling factor of 0.9914. Solvation free energies were computed using the COSMO-RS[88,89] method, that combines the conductor-like solvation model (COSMO) and statistical fluid thermodynamics, using the COSMO*therm23* software package.[90] Spin multiplicities of the ground electronic states were determined by rigorous comparison based on the arguments detailed in ref. 91 and references therein. The dependency of the spin-crossover energies on the exact exchange fraction was extracted by linear regression, using the BP86, PBE,[81,92] B3LYP*,[93-95] B3LYP and PBE0[81,92,96] functionals. One-dimensional PESs were calculated analogous to geometry optimizations. The exact position of a transition state pertaining to the electronic structure methods on a PES was determined from the Newton polynomial and confirmed by the presence of exactly one negative frequency.

Assessing the solvation free energy of a proton dissolved in acetonitrile under standard conditions is difficult with standard quantum chemical methods.[97] Thus, we utilize the experimental estimate of $\Delta_S G(H^+)$ = –260.2 kcal·mol^{-1} based on the cluster pair approximation.[98,99] Calculated pK_a values of all employed proton donors are listed in Table S1. As reduction potentials have been experimentally measured vs. Fc/Fc$^+$ reference, calculated reduction potentials are consistently displayed relative to an experimental reference of 4.96 V.[99–101] Finally, a correction of 1.9Δn kcal·mol^{-1} (corresponding to the difference between the concentration of the ideal gas at 298 K and 1 atm and its standard 1 mol·L^{-1} concentration at

the same pressure and temperature; Δn is the change in the number of moles in the reaction) has been applied so that the computed values refer to the 1 $mol \cdot L^{-1}$ standard state.

CONCLUSIONS

By combining electrochemical and kinetic measurements with quantum chemical calculations, we have elucidated the catalytic mechanism of CO_2 reduction by the heptacoordinated iron complex **FeL^{MeOH}** and identified the origin of the high selectivity towards the generation of CO. In addition, we have successfully applied the catalyst for selective CO_2 reduction to CO under light-driven catalytic conditions. In the presence of TFE as a proton donor, quantitative formation of CO is attained. Transient absorption spectroscopy measurements highlight that the rate-determining step in photochemical catalysis is represented by the electron transfer from the reduced sensitizer to **FeL^{MeOH}**, which results in decomposition pathways for the chromophore. Modulation of the light flux to reduce the amount of photogenerated reductant finally enables a dramatic improvement of the quantum efficiency of the reaction. These results point out the great potential of molecular catalysis to target selective generation of carbon-based products in CO_2RR and showcase the fundamental role of light as a reactant in tuning the efficiency of a photoreaction. We are certain that the synergistic combination of fast molecular catalysis and efficient photochemical reactions will definitely generate new avenues in the context of catalysis for solar fuel formation.

AUTHOR INFORMATION

Corresponding Authors

* M.N., mirco.natali@unife.it; A.R., albert.ruggi@unifr.ch, L.R., lubomir.rulisek@uochb.cas.cz

Author Contributions

F.D. performed the experimental studies that were planned and designed under the advice of A.R. and M.N.; F.L. carried out all quantum chemical calculations that were planned and designed with the help and advice of L.R. M.N. wrote the original draft and the manuscript was finalized through contributions of all authors. All authors have given approval to the final version of the manuscript.

ASSOCIATED CONTENT

Supporting Information. Computational data: coordinates of all stationary points and their respective energies (file type, ZIP). Additional electrochemical, computational, and photochemical data (file type, PDF). The following files are available free of charge.

ACKNOWLEDGEMENT

Emanuele Pattaro (University of Ferrara) is gratefully acknowledged for preliminary experiments. Marco Carmosino (University of Ferrara) is acknowledged for assistance. M.N. gratefully acknowledges financial support from the Italian MUR (PRIN2020, Electrolight4Value, 2020927WY3), from the European Union – Next Generation EU (PRIN2022 PNRR PHOTOCORE, P2022ZSPWF) and from the University of Ferrara (FAR2022, FAR2023). F.L. and L.R. acknowledge the support of the Ministry of Education, Youth and Sports of the Czech Republic (MSMT CR, LUAUS24230). A.R. acknowledges the Université de Fribourg (Pool de la recherche, project PO2325) for financial support.

REFERENCES

1 Morris, A.; Meyer, G. J.; Fujita, E. Molecular Approaches to the Photocatalytic Reduction of Carbon Dioxide for Solar Fuels. *Acc. Chem. Rev.* **2009**, *42*, 1983-1994. DOI: 10.1021/ar9001679.

2 White, J. L.; Baruch, M. F.; Pander III, J. E.; Hu, Y.; Fortmeyer, I. C.; Park, J. E.; Zhang, T.; Liao, K.; Gu, J.; Yan, Y.; Shaw, T. W.; Abelev, E.; Bocarsly, A. B. Light-Driven Heterogeneous Reduction of Carbon Dioxide: Photocatalysts and Photoelectrodes. *Chem. Rev.* **2015**, *115*, 12888-12935. DOI: 10.1021/acs.chemrev.5b00370.

3 Takeda, H.; Cometto, C.; Ishitani, O.; Robert, M. Electrons, Photons, Protons and Earth-Abundant Metal Complexes for Molecular Catalysis of CO_2 Reduction. *ACS Catal.* **2017**, *7*, 70-88. DOI: 10.1021/acscatal.6b02181.

4 Lamy, E.; Nadjo, L.; Savéant, J.-M. Standard Potential and Kinetic Parameters of the Electrochemical Reduction of Carbon Dioxide in Dimethylformamide. *J. Electroanal. Chem.* **1977**, *78*, 403-407. DOI: 10.1016/S0022-0728(77)80143-5.

5 Matsubara, Y.; Grills, D.; Kuwahara, Y. Thermodynamic Aspects of Electrocatalytic CO_2 Reduction in Acetonitrile and with an Ionic Liquid as Solvent or Electrolyte. *ACS Catal.* **2015**, *11*, 6440-6452. DOI: 10.1021/acscatal.5b00656.

6 Pegis, M. L.; Roberts, J. A. S.; Wasylenko, D. J.; Mader, E. A.; Appel, A. M.; Mayer, J. M. Standard Reduction Potentials for Oxygen and Carbon Dioxide Couples in Acetonitrile and *N*,*N*-Dimethylformamide. *Inorg. Chem.* **2015**, *54*, 11883-11888. DOI: 10.1021/acs.inorgchem.5b02136

7 Benson, E. E.; Kubiak, C. P.; Sathrum, A.; Smieja, J. M. Electrocatalytic and Homogeneous Approaches to Conversion of CO_2 to Liquid Fuels. *Chem. Soc. Rev.* **2009**, *38*, 89-99. DOI: 10.1039/B804323J.

8 Azcarate, I.; Constentin, C.; Robert, M.; Savéant, J.-M. Through-Space Charge Interaction Substituent Effects in Molecular Catalysis Leading to the Design of the Most Efficient Catalyst of CO_2-to-CO Electrochemical Conversion. *J. Am. Chem. Soc.* **2016**, *138*, 16639-16644. DOI: 10.1021/jacs.6b07014.

9 Derrick, J.-S.; Loipersberger, M.; Chatterjee, R.; Iovan, D. A.; Smith, P. T.; Chakarawet, K.; Yano, J.; Long, J. R.; Head-Gordon, M.; Chang, C. J. Metal−Ligand Cooperativity via Exchange Coupling Promotes Iron-Catalyzed Electrochemical CO_2 Reduction at Low Overpotentials. *J. Am. Chem. Soc.* **2020**, *142*, 20489-20501. DOI: 10.1021/jacs.0c10664.

10 De La Torre, P.; Derrick, J. S.; Snider, A.; Smith, P. T.; Loipersberger, M.; Head-Gordon, M.; Chang, C. J. Exchange Coupling Determines Metal-Dependent Efficiency for Iron- and Cobalt-Catalyzed Photochemical CO_2 Reduction. *ACS Catal.* **2022**, *12*, 8484-8493. DOI: 10.1021/acscatal.2c02072.

11 Elgrishi, N.; Chambers, M. B.; Wiang, X.; Fontecave, M. Molecular Polypyridine-Based Metal Complexes as Catalysts for the Reduction of CO_2. *Chem. Soc. Rev.* **2017**, *46*, 761-796. DOI: 10.1039/C5CS00391A.

12 Gonell, S.; Lloret-Fillol, J.; Miller, A. J. M. An Iron Pyridyl-Carbene Electrocatalyst for Low Overpotential CO_2 Reduction to CO. *ACS Catal*. **2021**, *11*, 615-626. DOI: 10.1021/acscatal.0c03798.

13 Guo, Z.; Chen, G.; Cometto, C.; Ma, B.; Zhao, H.; Groizard, T.; Chen, L.; Fan, H.; Man, W. L.; You, S. M.; Lau, K. C.; Lau, T. C.; Robert, M. Selectivity Control of CO versus $HCOO^-$ Production in the Visible-Light-Driven Catalytic Reduction of CO_2 with Two Cooperative Metal Sites. *Nat. Catal.* **2019**, *2*, 801-808. DOI: 10.1038/s41929-019-0331-6.

14 Bourrez, M.; Orio, M.; Molton, F.; Vezin, H.; Duboc, C.; Deronzier, A.; Chardon-Noblat, S. Pulsed-EPR Evidence of a Manganese(II) Hydroxycarbonyl Intermediate in the Electrocatalytic Reduction of Carbon Dioxide by a Manganese Bipyridyl Derivative. *Angew. Chem. Int. Ed.* **2014**, *53*, 240-243. DOI: 10.1002/anie.201306750.

15 Hooe, S. L.; Dressel, J. M.; Dickie, D. A.; Machan, C. W. Highly Efficient Electrocatalytic Reduction of CO_2 to CO by a Molecular Chromium Complex. *ACS Catal*. **2020**, *10*, 1146-1151. DOI: 10.1021/acscatal.9b04687.

16 Bonetto, R.; Altieri, R.; Tagliapietra, M.; Barbon, A.; Bonchio, M.; Robert, M.; Sartorel, A. Electrochemical Conversion of CO_2 to CO by a Competent Fe^{I} Intermediate Bearing a Schiff Base Ligand. *ChemSusChem* **2020**, *13*, 4111-4120. DOI: 10.1002/cssc.202001143.

17 a) Gracia, L. L.; Barani, E.; Braun, J.; Carter, A. B.; Fuhr, O.; Powell, A. K.; Fink, K.; Bizzarri, C. Photocatalytic Reduction of CO_2 by Highly Efficient Homogeneous Fe^{II} Catalyst based on 2,6-Bis(1',2',3'-triazolyl-methyl)pyridine. Comparison with Analogues. *ChemCatChem* **2022**, *14*, e202201163. DOI: 10.1002/cctc.202201163. b) Bizzarri, C. Homogeneous Systems Containing Earth-Abundant Metal Complexes for Photoactivated CO_2 Reduction: Recent Advances. *Eur. J. Org. Chem.* **2022**, e202200185. DOI: 10.1002/ejoc.202200185.

18 Saha, P.; Amanullah, S.; Dey, A. Selectivity in Electrochemical CO_2 Reduction. *Acc. Chem. Rev.* **2022**, *55*, 134-144. DOI: 10.1021/acs.accounts.1c00678.

19 Chen, L. Guo, Z.; Wei, X. G.; Gallenkamp, C.; Bonin, J.; Anxolabéhère-Mallart, E.; Lau, K. C.; Lau, T. C.; Robert, M. Molecular Catalysis of the Electrochemical and Photochemical Reduction of CO_2 with Earth-Abundant Metal Complexes. Selective Production of CO vs HCOOH by Switching of the Metal Center. *J. Am. Chem Soc*. **2015**, *137*, 10918-10921. DOI: 10.1021/jacs.5b06535.

20 Rodrigues, R. R.; Boudreaux, C. M.; Papish, E. T.; Delcamp, J. H. Photocatalytic Reduction of CO2 to CO and Formate: Do Reaction Conditions or Ruthenium Catalysts Control Product Selectivity? *ACS Appl. Energy Mater*. **2019**, *2*, 37-46. DOI: 10.1021/acsaem.8b01560.

21 Gracia, L. L., Henkel, P.; Fuhr, O.; Bizzarri, C. Selectivity Control Towards CO versus H_2 for Photo-Driven CO_2 Reduction with a Novel Co(II) Catalyst. *Beilstein J. Org. Chem*. **2023**, *19*, 1766-1775. DOI: 10.3762/bjoc.19.129.

22 Natali, M.; Badetti, E.; Deponti, E.; Gamberoni, M.; Scaramuzzo, F. A.; Sartorel, A.; Zonta, C. Photoinduced Hydrogen Evolution with New Tetradentate Cobalt(II) Complexes Based on the TPMA Ligand. *Dalton Trans.* **2016**, *45*, 14764-14773. DOI: 10.1039/C6DT01705C.

23 Carmo dos Santos, N. A.; Natali, M.; Badetti, E.; Wurst, K.; Licini, G.; Zonta, C. Cobalt, Nickel, and Iron Complexes of 8-hydroxyquinoline-di(2-picolyl)amine for Light-Driven Hydrogen Evolution. *Dalton Trans*. **2017**, *46*, 16455-16464. DOI: 10.1039/C7DT02666H.

24 Droghetti, F.; Begato, F.; Raulin, M.; Musiu, G.; Licini, G.; Natali, M.; Zonta, C. Strong Enhancement in Cobalt(II) TPMA Aqueous Hydrogen Photosynthesis through Intramolecular Proton Relay. *Angew. Chem., Int. Ed*. **2024**, e202408316. DOI: 10.1002/anie.202408316 .

25 Benazzi, E.; Begato, F.; Niorettini, A.; Destro, L.; Wurst, K.; Licini, G.; Agnoli, S.; Zonta, C.; Natali, M. Electrocatalytic Hydrogen Evolution Using Hybrid Electrodes Based on Single-Walled Carbon Nanohorns and Cobalt(II) Polypyridine Complexes. *J. Mater. Chem. A* **2021**, *9*, 20032-20039. DOI: 10.1039/D1TA03645A.

26 Droghetti, F.; Lucarini, F.; Molinari, A.; Ruggi, A.; Natali, M. Recent Findings and Future Directions in Photosynthetic Hydrogen Evolution Using Polypyridine Cobalt Complexes. *Dalton Trans*. **2022**, *51*, 10658-10673. DOI: 10.1039/D2DT00476C.

27 Lucarini, F.; Pastore, M.; Vasylevskyi, S.; Varisco, M.; Solari, E.; Crochet, A.; Fromm, K. M.; Zobi, F.; Ruggi, A. Heptacoordinate Co^{II} Complex: A New Architecture for Photochemical Hydrogen Production. *Chem. Eur. J*. **2017**, *23*, 6768-6771. DOI: 10.1002/chem.201701427.

28 Lucarini, F.; Fize, J.; Morozan, A.; Marazzi, M.; Natali, M.; Pastore, M.; Artero, V.; Ruggi, A. Insights into the Mechanism of Photosynthetic H_2 Evolution Catalyzed by a Heptacoordinate Cobalt Complex. *Sustain. Energy Fuels* **2020**, *4*, 589-599. DOI: 10.1039/C9SE00434C.

29 Lucarini, F.; Bongni, D.; Schiel, P.; Bevini, G.; Benazzi, E.; Solari, E.; Fadaei-Tirani, F.; Scopelliti, R.; Marazzi, M.; Natali, M.; Pastore, M.; Ruggi, A. Rationalizing Photo-Triggered Hydrogen Evolution Using Polypyridine Cobalt Complexes: Substituent Effects on Hexadentate Chelating Ligands. *ChemSusChem* **2021**, *14*, 1874-1885. DOI: 10.1002/cssc.202100161.

30 Orlando, A.; Lucarini, F.; Benazzi, E.; Droghetti, F.; Ruggi, A.; Natali, M. Rethinking Electronic Effects in Photochemical Hydrogen Evolution Using $CuInS_2$@ZnS Quantum Dots Sensitizers. *Molecules* **2022**, *27*, 8277. DOI: 10.3390/molecules27238277.

31 Lucarini, F.; Fize, J.; Morozan, A.; Droghetti, F.; Solari, E.; Scopelliti, R.; Marazzi, M.; Natali, M.; Pastore, M.; Artero, V.; Ruggi, A. Electro- and Photochemical H_2 Generation by Co(II) Polypyridyl-Based Catalysts Bearing Orthosubstituted Pyridines. *Sustain. Energy Fuels* **2023**, *7*, 3384-3394. DOI: 10.1039/D3SE00295K.

32 Droghetti, F.; Amati, A.; Ruggi, A.; Natali, M. Bioinspired Motifs in Proton and CO_2 Reduction with 3d-Metal Polypyridine Complexes. *Chem. Commun*. **2024**, *60*, 658-673. DOI: 10.1039/D3CC05156K.

33 Lubitz, W.; Ogata, H.; Rüdiger, O.; Reijerse, E. Hydrogenases. *Chem. Rev.* **2014**, *114*, 4081-4148. DOI: 10.1021/cr4005814.

34 Dey, S.; Das, P. K.; Dey, A. Mononuclear Iron Hydrogenase. *Coord. Chem. Rev*. **2013**, *257*, 42-63. DOI: 10.1016/j.ccr.2012.04.021.

35 Queyriaux, N. Redox-Active Ligands in Electroassisted Catalytic H^+ and CO_2 Reductions: Benefits and Risks. *ACS Catal.* **2021**, *11*, 4024-4035. DOI: 10.1021/acscatal.1c00237.

36 Nicolet, Y.; Ogata, H.; Miki, K.; Yasuoka, N.; Yagi, T. Desulfovibrio Desulfuricans Iron Hydrogenase: The Structure Shows Unusual Coordination to an Active Site Fe Binuclear Center. *Structure* **1999**, *7*, 13-23. DOI: 10.1016/s0969-2126(99)80005-7.

37 Droghetti, F.; Amati, A.; Pascale, F.; Crochet, A.; Pastore, M.; Ruggi, A.; Natali, M. Catalytic CO_2 Reduction with Heptacoordinated Polypyridine Complexes: Switching the Selectivity via Metal Replacement. *ChemSusChem* **2024**, *17*, e202300737. DOI: 10.1002/cssc.202300737.

38 Khobragade, D. A.; Mahamulkar, S. G.; Pospíšil, L.; Císařová, I.; Rulíšek, L.; Jahn, U. Acceptor-Substituted Ferrocenium Salts as Strong, Single-Electron Oxidants: Synthesis, Electrochemistry, Theoretical Investigations, and Initial Synthetic Application. *Chem. Eur. J.* **2012**, *18*, 12267-12277. DOI: 10.1002/chem.201201499.

39 Tomaník, L.; Rulíšek, L.; Slavíček, P. Redox Potentials with COSMO-RS: Systematic Benchmarking with Different Databases. *J. Chem. Theory Comput.* **2023**, *19*, 1014-1022. DOI: 10.1021/acs.jctc.2c00919.

40 Bím, D.; Chalupský, J.; Culka, M.; Solomon, E. I.; Rulíšek, L.; Srnec, M. Proton–Electron Transfer to the Active Site is Essential for the Reaction Mechanism of Soluble Δ^9-Desaturase. *J. Am. Chem. Soc.* **2020**, *142*, 10412-10423. DOI: 10.1021/jacs.0c01786.

41 Bím, D.; Rulíšek, L.; Srnec, M. Computational Electrochemistry as a Reliable Probe of Experimentally Elusive Mononuclear Nonheme Iron Species. *J. Phys. Chem. C* **2018**, *122*, 10773-10782. DOI: 10.1021/acs.jpcc.8b02698.

42 Andris, E.; Segers, K.; Mehara, J.; Rulíšek, L.; Roithová, J. Closed Shell Iron(IV) Oxo Complex with an Fe–O Triple Bond: Computational Design, Synthesis, and Reactivity. *Angew. Chem. Int. Ed.* **2020**, *59*, 23137-23144. DOI: 10.1002/anie.202009347.

43 Loipersberger, M.; Derrick, J. S.; Chang, C. J.; Head-Gordon, M. Deciphering Distinct Overpotential-Dependent Pathways for Electrochemical CO_2 Reduction Catalyzed by an Iron−Terpyridine Complex. *Inorg. Chem.* **2022**, *61*, 6919-6933. DOI: 10.1021/acs.inorgchem.2c00279.

44 Wang, X.-Z.; Meng, S.-L.; Chen, J.-Y.; Wang, H.-X., Wang, Y.; Zhou, S.; Li, X.-B.; Liao, R.-Z.; Tung, C.-H.; Wu, L.-Z. Mechanistic Insights into Iron(II) Bis(pyridyl)amine-Bipyridine Skeleton for Selective CO_2 Photoreduction. *Angew. Chem. Int. Ed*. **2021**, *60*, 26072-26079. DOI: 10.1002/anie.202107386.

45 McCarthy, B. D.; Martin, D. J.; Rountree, E. S.; Ullman, A. C.; Dempsey, J. L. Electrochemical Reduction of Brønsted Acids by Glassy Carbon in Acetonitrile - Implications for Electrocatalytic Hydrogen Evolution. *Inorg. Chem.* **2014**, *53*, 8350-8361. DOI: 10.1021/ic500770k.

46 Constentin, C.; Savéant, J.-M. Multielectron, Multistep Molecular Catalysis of Electrochemical Reactions: Benchmarking of Homogeneous Catalysts. *ChemElectroChem* **2014**, *1*, 1226-1236. DOI: 10.1002/celc.201300263.

47 Lam, Y. C.; Nielsen, R. J.; Gray, H. B.; Goddard, W. A. A Mn Bipyrimidine Catalyst Predicted to Reduce CO_2 at Lower Overpotential. *ACS Catal.* **2015**, *5*, 2521-2528. DOI: 10.1021/cs501963v.

48 Fourmond, V.; Jacques, P. A.; Fontecave, M.; Artero, V. H_2 Evolution and Molecular Electrocatalysts: Determination of Overpotentials and Effect of Homoconjugation. *Inorg. Chem*. **2010**, *49*, 10338-10347. DOI: 10.1021/ic101187v

49 Fernandez, S.; Franco, F.; Casadevall, C.; Martin-Diaconescu, V.; Luis, J. M.; Lloret-Fillol, J. A Unified Electro- and Photocatalytic CO_2 to CO Reduction Mechanism with Aminopyridine Cobalt Complexes. *J. Am. Chem. Soc.* **2020**, *142*, 120-133. DOI: 10.1021/jacs.9b06633.

50 Bonetto, R.; Crisanti, F.; Sartorel, A. Carbon Dioxide Reduction Mediated by Iron Catalysts: Mechanism and Intermediates That Guide Selectivity. *ACS Omega* **2020**, *5*, 21309-21319. DOI: 10.1021/acsomega.0c02786.

51 The involvement of a double protonated ligand can be ruled out based on thermodynamic arguments. Calculation of a plausible $^5[H_{S1}H_{S2}LFe]^{2+}$ intermediate indeed indicates that this species is considerably less stable by more than 12 kcal·mol^{-1} with respect to either of the two structures with one proton on the ligand and one at the metal center.

52 We wish to highlight that this procedure enables a fairer estimation of the quantum yield with respect to that previously employed, as the present one can take into account any potential influence determined by the reactor geometry.

53 Lehn, J. M.; Ziessel, R. Photochemical Reduction of Carbon Dioxide to Formate Catalyzed by 2,2'-Bipyridine- or 1,10-Phenanthroline-Ruthenium(II) Complexes. *J. Organometall. Chem*. **1990**, *382*, 157-173. DOI: 10.1016/0022-328X(90)85224-M.

54 Shimoda, T.; Morishima, T.; Kodama, K.; Hirose, T.; Polyansky, D. E.; Manbeck, G. F.; Muckerman, J. T.; Fujita, E. Photocatalytic CO_2 Reduction by Trigonal-Bipyramidal Cobalt(II) Polypyridyl Complexes: The Nature of Cobalt(I) and Cobalt(0) Complexes upon

Their Reactions with CO_2, CO, or Proton. *Inorg. Chem*. **2018**, *57*, 5486-5498. DOI: 10.1021/acs.inorgchem.8b00433.

55 Fortage, J.; Collomb, M.-N.; Costentin, C. Turnover Number in Photoinduced Molecular Catalysis of Hydrogen Evolution: A Benchmarking for Catalysts? *ChemSusChem* **2024**, *17*, e202400205. DOI: 10.1002/cssc.202400205.

56 Wang, J. W.; Li, Z.; Luo, Z. M.; Huang, Y.; Kupfer, S.; Ouyang, G. Boosting CO_2 Photoreduction by π–π-induced Preassembly between a Cu(I) Sensitizer and a Pyrene-Appended Co(II) Catalyst. *Proc. Natl. Acad. Sci.* **2023**, *120*, e2221219120. DOI: 10.1073/pnas.2221219120.

57 Wang, J. W.; Zhang, X.; Velasco, L.; Karnhal, M.; Li, Z.; Luo, Z. M.; Huang, Y.; Yu, J.; Hu, W.; Zhang, X.; Yamauchi, K.; Sakai, K.; Moonshiram, D.; Ouyang, G. Precious-Metal-Free CO_2 Photoreduction Boosted by Dynamic Coordinative Interaction between Pyridine-Tethered Cu(I) Sensitizers and a Co(II) Catalyst. *JACS Au* **2023**, *3*, 1984-1997. DOI: 10.1021/jacsau.3c00218.

58 Ho, P. Y.; Cheng, S. C.; Yu, F.; Yeung, Y. Y.; Ni, W. X.; Ko, C. C.; Leung, C. F.; Lau, T. C.; Robert, M. Light-Driven Reduction of CO_2 to CO in Water with a Cobalt Molecular Catalyst and an Organic Sensitizer. *ACS Catal.* **2023**, *13*, 5979-5985. DOI: 10.1021/acscatal.3c00036.

59 Krishnan, C. V.; Sutin, N. Homogeneous Catalysis of the Photoreduction of Water by Visible Light. 2. Mediation by a Tris(2,2'-bipyridine)ruthenium(II)-Cobalt(II) Bipyridine System. *J. Am. Chem. Soc.* **1981**, *103*, 2141-2142. DOI: 10.1021/ja00398a066.

60 Pellegrin, Y.; Odobel, F. Sacrificial Electron Donor Reagents for Solar Fuel Production. *C. R. Chim*. **2017**, *20*, 283-295. DOI: 10.1016/j.crci.2015.11.026.

61 Deponti, E.; Luisa, A.; Natali, M.; Iengo, E.; Scandola, F. Photoinduced Hydrogen Evolution by a Pentapyridine Cobalt Complex: Elucidating Some Mechanistic Aspects. *Dalton Trans.* **2014**, *43*, 16345-16353. DOI: 10.1039/C4DT02269F.

62 Natali, M.; Orlandi, M.; Berardi, S.; Campagna, S.; Bonchio, M.; Sartorel, A.; Scandola, F. Photoinduced Water Oxidation by a Tetraruthenium Polyoxometalate Catalyst: Ion-pairing and Primary Processes with $Ru(bpy)_3^{2+}$ Photosensitizer. *Inorg. Chem.* **2012**, *51*, 7324-7331. DOI: 10.1021/ic300703f.

63 Juris, A.; Balzani, V.; Barigelletti, F.; Campagna, S.; Belser, P.; Von Zelewsky, A. Ru(II) Polypyridine Complexes: Photophysics, Photochemistry, Eletrochemistry, and Chemiluminescence. *Coord. Chem. Rev.* **1988**, *84*, 85-277. DOI: 10.1016/0010-8545(88)80032-8.

64 The cage escape yield can be estimated from the ratio between the amount of $[Ru(bpy)_3]^+$ calculated from the ΔOD at 500 nm of the spectrum at 2 μs with the corresponding $\Delta\varepsilon$ = 9000 $M^{-1}cm^{-1}$ and the amount of $^3*[Ru(bpy)_3]^{2+}$ calculated from the ΔOD at 370 nm of the prompt spectrum (blue trace) with the corresponding $\Delta\varepsilon$ = 18000 $M^{-1}cm^{-1}$, then accounting for the stoichiometry of the reaction as two $[Ru(bpy)_3]^+$ are attained per absorbed photons.

65 Volpe, A.; Tubaro, C.; Natali, M.; Sartorel, A.; Brudvig, G. W.; Bonchio, M. Light-Driven Water Oxidation with the Ir-blue Catalyst and the $Ru(bpy)_3^{2+}/S_2O_8^{2-}$ Cycle: Photogeneration of Active Dimers, Electron-Transfer Kinetics, and Light Synchronization for Oxygen Evolution with High Quantum Efficiency. *Inorg. Chem.* **2019**, *58*, 16537-16545. DOI: 10.1021/acs.inorgchem.9b02531.

66 Volpe, A.; Natali, M.; Graiff, C.; Sartorel, A.; Tubaro, C.; Bonchio, M. Novel Iridium Complexes with N-heterocyclic Dicarbene Ligands in Light-Driven Water Oxidation Catalysis: Photon Management, Ligand Effect and Catalyst Evolution. *Dalton Trans.* **2020**, *49*, 2696-2705. DOI: 10.1039/C9DT04841C.

67 Rossin, E.; Bonchio, M.; Natali, M.; Sartorel, A. Sequential Proton Coupled Electron Transfer Events from a Tetraruthenium Polyoxometalate in Photochemical Water Oxidation. *Sustain. Energy Fuels* **2024**, *8*, 1944-1952. DOI: 10.1039/D4SE00146J.

68 Tanaka, S.; Annaka, M.; Sakai, K. Visible Light-Induced Water Oxidation Catalyzed by Molybdenum-Based Polyoxometalates with Mono- and Dicobalt(III) Cores as Oxygen-Evolving Centers. *Chem. Commun*. **2012**, *48*, 1653-1655. DOI: 10.1039/C2CC16821A.

69 Connell, T. U. The Forgotten Reagent of Photoredox Catalysis. *Dalton Trans.* **2022**, *51*, 13176-13188. DOI: 10.1039/D2DT01491B.

70 Reiss, B.; Hu, Q.; Riedle, E.; Wagenknecht, H. A. The Dependence of Chemical Quantum Yields of Visible Light Photoredox Catalysis on the Irradiation Power. *ChemPhotoChem* **2021**, *5*, 1009-1019. DOI: 10.1002/cptc.202100090.

71 Walden, S. L.; Carroll, J. A.; Unterreiner, A. N.; Barner-Kowolik, C. Photochemical Action Plots Reveal the Fundamental Mismatch Between Absorptivity and Photochemical Reactivity. *Adv. Sci.* **2024**, *11*, 2306014. DOI: 10.1002/advs.202306014.

72 Connelly, N. G.; Geiger, W. E. Chemical Redox Agents for Organometallic Chemistry. *Chem. Rev.* **1996**, *96*, 877-910. DOI: 10.1021/cr940053x.

73 Balasubramani, S. G.; Chen, G. P.; Coriani, S.; Diedenhofen, M.; Frank, M. S.; Franzke, Y. J.; Furche, F.; Grotjahn, R.; Harding, M. E.; Hättig, C.; Hellweg, A.; Helmich-Paris, B.; Holzer, C.; Huniar, U.; Kaupp, M.; Marefat Khah, A.; Karbalaei Khani, S.; Müller, T.; Mack, F.; Nguyen, B. D.; Parker, S. M.; Perlt, E.; Rappoport, D.; Reiter, K.; Roy, S.; Rückert, M.; Schmitz, G.; Sierka, M.; Tapavicza, E.; Tew, D. P.; van Wüllen, C.; Voora, V. K.; Weigend, F.; Wodyński, A.; Yu, J. M. Turbomole: Modular Program Suite for Ab Initio Quantum-Chemical and Condensed-Matter Simulations. *J. Chem. Phys*. **2020**, *152*, 184107. DOI: 10.1063/5.0004635.

74 Grimme, S.; Antony, J.; Ehrlich, S.; Krieg, H. A Consistent and Accurate Ab Initio Parametrization of Density Functional Dispersion Correction (DFT-D) For The 94 Elements H-Pu. *J. Chem. Phys.* **2010**, *132*, 154104. DOI: 10.1063/1.3382344.

75 Grimme, S.; Ehrlich, S.; Goerigk, L. Effect of The Damping Function in Dispersion Corrected Density Functional Theory. *J. Comp. Chem*. **2011**, *32*, 1456-1465. DOI: 10.1002/jcc.21759.

76 Becke, A. D.; Johnson, E. R. A Density-Functional Model of the Dispersion Interaction. *J. Chem. Phys.* **2005**, *122*, 54101. DOI: 10.1063/1.2065267.

77 Johnson, E. R.; Becke, A. D. A Post-Hartree–Fock Model of Intermolecular Interactions. *J. Chem. Phys.* **2005**, *123*, 024101. DOI: 10.1063/1.1949201.

78 Johnson, E. R.; Becke, A. D. A Post-Hartree-Fock Model of Intermolecular Interactions: Inclusion of Higher-Order Corrections. *J. Chem. Phys*. **2006**, *124*, 174104. DOI: 10.1063/1.2190220.

79 Becke, A. D. Density-Functional Exchange-Energy Approximation with Correct Asymptotic Behavior. *Phys. Rev. A* **1988**, *38*, 3098-3100. DOI: 10.1103/PhysRevA.38.3098.

80 Perdew, J. P. Density-Functional Approximation for the Correlation Energy of the Inhomogeneous Electron Gas. *Phys. Rev. B* **1986**, *33*, 8822-8824. DOI: 10.1103/PhysRevB.33.8822.

81 Slater, J. C. A Simplification of the Hartree-Fock Method. *Phys. Rev*. **1951**, *81*, 385-390. DOI: 10.1103/PhysRev.81.385.

82 Vosko, S. H.; Wilk, L.; Nusair, M. Accurate Spin-Dependent Electron Liquid Correlation Energies for Local Spin Density Calculations: A Critical Analysis. *Can. J. Phys.* **1980**, *58*, 1200-1211. DOI: 10.1139/p80-159.

83 Lee, C.; Yang, W.; Parr, R. G. Development of the Colle-Salvetti Correlation-Energy Formula into a Functional of the Electron Density. *Phys. Rev. B* **1988**, *37*, 785-789. DOI: 10.1103/PhysRevB.37.785.

84 Stephens, P. J.; Devlin, F. J.; Chabalowski, C. F.; Frisch, M. J. Ab Initio Calculation of Vibrational Absorption and Circular Dichroism Spectra Using Density Functional Force Fields. *J. Phys. Chem.* **1994**, *98*, 11623-11627. DOI: 10.1021/j100096a001.

85 Mardirossian, N.; Head-Gordon, M. ωB97M-V: A Combinatorially Optimized, Range-Separated Hybrid, Meta-GGA Density Functional with VV10 Nonlocal Correction. *J. Chem. Phys.* **2016**, *144*, 214110. DOI: 10.1063/1.4952647.

86 Vydrova, O. L.; Van Voorhis, T. Nonlocal Van Der Waals Density Functional: The Simpler the Better. *J. Chem. Phys*. **2010**, *133*, 244103. DOI: 10.1063/1.3521275.

87 Bannwarth, C.; Caldeweyher, E.; Ehlert, S.; Hansen, A.; Pracht, P.; Seibert, J.; Spicher, S.; Grimme, S. Extended Tight-Binding Quantum Chemistry Methods WIREs *Comput. Mol. Sci.* **2020**, *11*, e1493.

88 Klamt, A.; Jonas, V.; Burger, T.; Lohrenz, J. C. W. Refinement and Parametrization of COSMO-RS. *J. Phys. Chem. A* **1998**, *102*, 5074-5085. DOI: 10.1002/wcms.1493.

89 Eckert, F.; Klamt, A. Fast Solvent Screening via Quantum Chemistry: COSMO-RS Approach. *AIChE J.* **2002**, *48*, 369-385. DOI: 10.1002/aic.690480220

90 Eckert, F.; Klamt, A. COSMOtherm, Version C2.1, Release 01.10; COSMOlogic GmbH & Co KG, Leverkusen, Germany, **2009**.

91 Bowman, D. N.; Jakubikova, E. Low-Spin versus High-Spin Ground State in Pseudo-Octahedral Iron Complexes. *Inorg. Chem*. **2012**, *51*, 6011-6019. DOI: 10.1021/ic202344w.

92 Perdew, J. P.; Burke, K.; Ernzerhof, M. Generalized Gradient Approximation Made Simple. *Phys. Rev. Lett*. **1996**, *77*, 3865-3868. DOI: 10.1103/PhysRevLett.77.3865.

93 Reiher, M.; Salomon, O.; Artur Hess, B. Reparameterization of Hybrid Functionals Based on Energy Differences of States of Different Multiplicity. *Theor. Chem. Acc*. **2001**, *107*, 48-55. DOI: 10.1007/s00214-001-0300-3.

94 Salomon, O.; Reiher, M.; Hess, B. A. Assertion of the Performance of the B3LYP* Functional for the First Transition Metal Row and the G2 Test Set. *J. Chem. Phys*. **2002**, *117*, 4729-4737. DOI: 10.1063/1.1493179.

95 Becke, A. D. Density-Functional Thermochemistry. III. The Role of Exact Exchange. *J. Chem. Phys.* **1993**, *98*, 5648-5652. DOI: 10.1063/1.464913.

96 Adamo, C.; Barone, V. Toward Reliable Density Functional Methods Without Adjustable Parameters: The PBE0 Model. *J. Chem. Phys.* **1999**, *110*, 6158-6170. DOI: 10.1063/1.478522.

97 Alongi, K. S.; Shields, G. C.; Wheeler, R. A. In Chapter 8 – Theoretical Calculations of Acid Dissociation Constants: A Review Article. *Annual Reports in Computational Chemistry* **2010**, *6*, 113-138. DOI: 10.1016/S1574-1400(10)06008-1.

98 Khobragade, D. A.; Mahamulkar, S. G.; Pospíšil, L.; Císařovμ, I.; Rulíšek, L.; Jahn, U. Acceptor-Substituted Ferrocenium Salts as Strong Single-Electron Oxidants: Synthesis, Electrochemistry, Theoretical Investigations, and Initial Synthetic Application. *Chem. Eur. J.* **2012**, *18*, 12267-12277. DOI: 10.1002/chem.201201499.

99 Kelly, C. P.; Cramer, C. J.; Truhlar, D. G. Single-Ion Solvation Free Energies and the Normal Hydrogen Electrode Potential in Methanol, Acetonitrile, and Dimethyl Sufoxide. *J. Phys. Chem. B* **2007**, *2*, 408-422. DOI: 10.1021/jp065403l.

100 Kastenholz, M. A.; Hünenberger, H. J. Computation of Methodology-Independent Ionic Solvation Free Energies from Molecular Simulations. II. The Hydration Free Energy of the Sodium Cation. *Chem. Phys.* **2006**, *124*, 224501. DOI: 10.1063/1.2201698.

101 Ben-Naim, A. Solvation Thermodynamics; Plenum: New York, **1987**. DOI: 10.1007/978-1-4757-6550-2.